Novel Polymeric Waveguides Optimized for Nanocrystal Hosting

M.Sc. Thesis

by

Yaron Glazer

This work was done under the supervision of

Dr. Dan Marom

The Selim and Rachel Benin School of Engineering,
The Hebrew University of Jerusalem.

June 2, 2009

Dedication

This thesis is dedicated to my wife, Sari, for being supportive and for standing by my side through the Master years.

Acknowledgments

First and foremost, I would like to thank Dr. Dan Marom for his guidance and advice throughout my master project. Special thanks to Noa Mazurski for her help and advice. I would also like to thank all the group members, Asael Adler, Ami Mizrahi, Amitay Rudnick, David Sinefeld, Drori Shayovitz, Jonathan Dunayevsky and Yoram Palti for their friendship and for sharing their knowledge with me.

This work is done in collaboration with Prof. Uri Banin of the Department of Physical Chemistry, The Hebrew University of Jerusalem, Israel. The assistance of his student, Assaf Aharoni, is gratefully acknowledged.

During this project, we were the first users of the new Nanofabrication Unit in the Hebrew University, and we were happy to be the startup seeds. During the last two years we helped accessorizing the unit and defining working and safety protocols. I would like to thank all the clean room staff for the support.

I would like to thank Intel Israel for their donation to the Nanofabrication Unit where I worked as a student during the first two years of the master.

Last but not least, I would like to thank my family for supporting me through my academic years.

Abstract

At the last decade, the wide growth in data transfer realized the requirement of optical communications for its high capacity capabilities. The revolution of optical communications has been enabled by the availability of ultra-low-loss silica fiber, which has also been the basis for a wide variety of optical building blocks.

Fabricating passive optical devices from high purity silica and glass, or fabricating active devices that utilize the direct band gap of semiconductors (SC) are relatively costly; therefore alternative solutions are being studied widely.

Our research is aiming to realize a platform based on passive polymer materials as the wave-guiding material, and in the future to dope it with SC nanocrystals (NC). Plastic (polymers) optical fiber has already found significant application in the Datacom market.

In this work we present the design of optical devices and their fabrication. Polymer selection is critical, as most polymers have CO and CH absorption bands which reside near 1.55μm wavelength. A PFCB core and a Cytop as cladding were chosen and combined together for the first time. This two polymers combination offers a very small attenuation at the optical communication wavelength of 1.55μm, high Δn and solubility with NC.

At the design process, we focused on realizing devices that will help us extract the basic characteristic of our polymer platform, such as propagation losses, bend losses and reflective index changes that will occur after NC doping.

Realizing polymeric waveguides with a micron-scale cross section of and length of a few centimeters has low defect tolerance which requires careful treatment. Fabrication was done with standard semiconductor process, such as lithography, reactive ion etching etc. Furthermore, a low preparation temperature is critical when heat-sensitive elements, such as semiconductors nanocrystals, are to be embedded in the waveguide. Finally, after the process development, we have the desired polymeric waveguide structure. This waveguide platform is now ready for future study of NC dopants.

Contents

Chapter 1

Theoretical Background

1.1 Motivation

Optical communications require the use of both active and passive optical devices. Passive devices are often fabricated in silica due to its intrinsic low absorption and simple processing, while many active devices utilize direct bandgap (BG) semiconductors (SC) due to their absorption and gain properties. Our research is aiming to realize a platform based on passive polymer materials as the wave guiding material, and dope it with SC nanocrystals (NC). This will allow us to create a long interaction region between the light and the SC NCs, and thus utilize the SC NC's optical properties for gain and absorption – both linear and non-linear.

The requirement from the polymeric host material is to have low absorption around the 1.55μm wavelength range and to have chemical compatibility with the SC NCs, to allow high loading ratios. Most polymers have CO and CH absorption bands which reside near 1.55μm wavelength. Our approach is to use perflourinated polymer in which the Fluorine has replaced most of the Oxygen and Hydrogen atoms, and thus has low absorption for the relevant wavelengths. We have designed and fabricated the waveguides with a small optical mode cross-section area, to allow for higher intensities and earlier onset of non-linear effects. This is done by controlling the refractive index of the core and cladding materials. Additional design requirements

are easy processing and high coupling efficiencies to single mode fibers – for which circular cross-section is preferred.

We have identified and started testing suitable polymeric host materials – PFCB (Perflourinated Cyclo-Butane) for the core material and Cytop™ (Poly (perfluorobutenylvinyl ether)) as cladding. Both have very low IR absorption. Additionally, compatibility of PFCB to NC allow high loading ratio (up to 20%), as has been demonstrated by others. This polymer combination allows us to create reflective index difference of ~10%, which allows single mode operation with mode diameter of ~1.5μm (FWHM) and effective beam cross section of ~5 μm^2. With this high beam confinement, a 1W CW optical beam can achieve photon fluxes of ~1 photon/(ps·nm^2) [11] [12] [13] [14].

We wish to disperse SC quantum dots (QD) and nanorods (NR) into the waveguide core region. Some of the interesting SC materials to explore for our application are those that have a direct bandgap at 1.55μm (such as InAs) or at ~0.8μm (such as PbSe).

1.2 Optical Waveguide Theory

Optical waveguides are used in various scientific and commercial applications to carry lightwaves in the visible and IR portions of the electromagnetic spectrum. Optical waveguides are typically constructed from dielectric material with high refractive index surrounded by a material with a lower refractive index. There are two approaches for analyzing of light propagation in optical waveguide: Rays and fields We focus on the latter using Maxwell's equations with boundary conditions to obtain the different modes of propagation in a rectangular waveguide [1].

1.2.1 Rectangular Waveguide

1.2.1.1 Basic Equations

In this section the wave analysis is described for the rectangular waveguide (Figure 1), with the method proposed by Marcatili [1]. The important assumption of this method is that the electromagnetic field can be neglected (gray area in Figure 1).

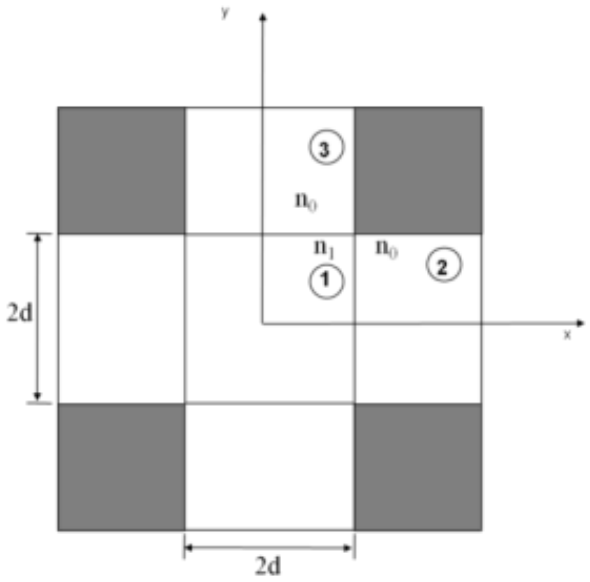

Figure 1: Three-dimensional rectangular waveguide

Taking into account the fact that we treat dielectric optical waveguide, we present the Maxwell's equations for homogeneous, linear and lossless dielectric medium in the terms of electric field E and magnetic field H.

$$\nabla \times \vec{E} = -\mu_0 \frac{\partial \vec{H}}{\partial t} \tag{1.1a}$$

$$\nabla \times \vec{H} = \varepsilon_0 n^2 \frac{\partial \vec{E}}{\partial t} \tag{1.1b}$$

Where ϵ_o and μ_o denote the permittivity and permeability of the medium, respectively. n is the refractive index. Let's assume that the electric field is monochromatic and propagate primarily in the z direction, i.e.

$$\vec{E} = \vec{\mathrm{E}}(\mathrm{x}, \mathrm{y})\mathrm{e}^{\mathrm{j}(\omega t - \beta z)} \tag{1.2a}$$

$$\vec{H} = \vec{\mathrm{H}}(\mathrm{x}, \mathrm{y})\mathrm{e}^{\mathrm{j}(\omega t - \beta z)} \tag{1.2b}$$

Substituting Eqs. (1.2a) and (1.2b) into Esq. (1.1a) and (1.1b) the following set of equations are obtained

$$\frac{\partial^2 H_x}{\partial x^2}+\frac{\partial^2 H_x}{\partial y^2}+(k^2n^2-\beta^2)H_x=0 \qquad \frac{\partial^2 H_y}{\partial x^2}+\frac{\partial^2 H_y}{\partial y^2}+(k^2n^2-\beta^2)H_y=0$$

$$\begin{cases} H_y=0 \\ E_x=\dfrac{1}{\omega\varepsilon_0 n^2\beta}\dfrac{\partial^2 H_x}{\partial x\partial y} \\ E_y=\dfrac{\omega\mu_0}{\beta}H_x-\dfrac{1}{\omega\varepsilon_0 n^2\beta}\dfrac{\partial^2 H_x}{\partial y^2} \\ E_z=\dfrac{j}{\omega\varepsilon_0 n^2}\dfrac{\partial H_x}{\partial y} \\ H_z=\dfrac{-j}{\beta}\dfrac{\partial H_x}{\partial x} \end{cases} \qquad \begin{cases} H_x=0 \\ E_x=\dfrac{\omega\mu_0}{\beta}H_y+\dfrac{1}{\omega\varepsilon_0 n^2\beta}\dfrac{\partial^2 H_y}{\partial x^2} \\ E_y=\dfrac{1}{\omega\varepsilon_0 n^2\beta}\dfrac{\partial^2 H_y}{\partial x\partial y} \\ E_z=\dfrac{-j}{\omega\varepsilon_0 n^2}\dfrac{\partial H_y}{\partial x} \\ H_z=\dfrac{-j}{\beta}\dfrac{\partial H_y}{\partial y} \end{cases}$$

(1.3) (1.4)

We see the solution is separable to one set where *Ey*, *Hx* are dominant, and another set where *Ex*, *Hy* are dominant.

The solution for *Ex* dominant can be express as

$$H_y=\begin{cases} A\cos(k_x x-\phi)\cos(k_y y-\psi) & region\ 1 \\ A\cos(k_x d-\phi)e^{-\gamma_x(x-a)}\cos(k_y y-\psi) & region\ 2 \\ A\cos(k_x x-\phi)e^{-\gamma_y(y-a)}\cos(k_y d-\psi) & region\ 3 \end{cases} \qquad (1.5)$$

Hy is oscillatory in the core and decaying in the cladding.

Where the transverse wavenumber κ_x , κ_y, γ_x and γ_y and the optical phases ϕ and ψ are given by

$$\begin{cases} -k_x^2-k_y^2+k^2n_1^2-\beta^2=0 & region\ 1 \\ \gamma_x^2-k_y^2+k^2n_1^2-\beta^2=0 & region\ 2 \\ -k_x^2+\gamma_y^2+k^2n_1^2-\beta^2=0 & region\ 3 \end{cases} \qquad (1.6)$$

$$\Rightarrow \beta=\sqrt{k^2n_1^2-(k_x^2+k_y^2)}$$

and

$$\begin{cases} \phi=(p-1)\dfrac{\pi}{2} & (p=1,2...) \\ \psi=(q-1)\dfrac{\pi}{2} & (q=1,2...) \end{cases} \qquad (1.7)$$

When we apply the boundary conditions for the electric field E_z at x=d and for the magnetic field E^x_{pq} for y=d we obtain the following dispersion equation:

$$k_x a = (p-1)\frac{\pi}{2} + \tan^{-1}\left(\frac{n_1^2 \gamma_x}{n_0^2 k_x}\right) \tag{1.8}$$

$$k_y a = (q-1)\frac{\pi}{2} + \tan^{-1}\left(\frac{\gamma_y}{k_y}\right) \tag{1.9}$$

As we are determining the fields for a symmetrical waveguide, the dispersion equation for E^y_{pq} is give by

$$k_x a = (p-1)\frac{\pi}{2} + \tan^{-1}\left(\frac{\gamma_x}{k_x}\right) \tag{1.10}$$

$$k_y a = (q-1)\frac{\pi}{2} + \tan^{-1}\left(\frac{n_1^2 \gamma_y}{n_0^2 k_y}\right) \tag{1.11}$$

1.2.1.1 Limitations in Marcatili's approach

Kumar et al, [1], proposed an improvement in accuracy for Marcatili's method by taking into account the contribution of the fields in the gray area in Figure 2. In this method the refractive index distribution is expressed by

$$n^2(x,y) = N_x^2(x) + N_y^2(y) - O\left(n_1^2 - n_0^2\right) \tag{1.12}$$

$$\begin{aligned} N_x^2(x) &= \begin{cases} n_1^2/2 & |x| \le d \\ n_0^2 - n_1^2/2 & |x| \ge d \end{cases} \\ N_y^2(y) &= \begin{cases} n_1^2/2 & |y| \le d \\ n_0^2 - n_1^2/2 & |y| \ge d \end{cases} \end{aligned} \tag{1.13}$$

In Figure 2 we can see the refractive index distribution that is expressed above.

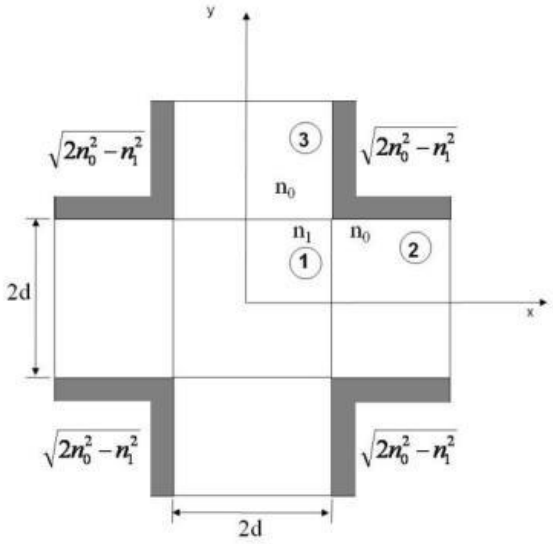

Figure 2: Refractive index profile in Kumar's method

Generally, the refractive index difference between core and cladding is quite small ($n_1 \approx n_0$), and then we have $O(n_1 - n_0) \approx 0$ in Eq. (1.12). The refractive index in the grey area is approximated as

$$\sqrt{2n_0^2 - n_1^2} \approx n_0 \tag{1.14}$$

Here solving the wave equation (1.3) for E^x_{pq} mode is done by using the separation of variables method, as

$$H_y(x,y) = X(x)Y(y) \tag{1.15}$$

Substituting Eqs.(1.2a)(1.12) and (1.15) into Eq. (1.3) the wave equation is reduced to

$$\frac{\partial^2 X}{\partial x^2} Y + \frac{\partial^2 Y}{\partial y^2} X + \left[k^2\left(N_x^2 + N_y^2\right) - \beta^2\right) XY\right] = 0 \tag{1.16}$$

The dispersion equations derived from this method are known to be the same as Eqs. (1.8) - (1.11), by Marcatili's method. But in Kumar's method, an improvement in the accuracy of the propagation constant can be obtained by the perturbation method. To do so the refractive index distribution is expressed as

$$n^2(x,y) = N_x^2(x) + N_y^2(y) - \delta\eta(x,y) \tag{1.17}$$

Where δ is a small quantity and $\delta\eta(x,y)$ is the propagation term. Generally the wave equation is expressed by

$$\begin{aligned} &\nabla^2 f + \left(k^2 n^2 - \beta^2\right) f = 0 \\ &\begin{cases} f = f_0 + \delta f_1 \\ \beta^2 = \beta_0^2 + \delta\beta_1^2 \end{cases} \end{aligned} \tag{1.18}$$

The eigenvalue that is given by the first-order perturbation is then expressed by

$$\beta^2 = \beta_0^2 + \frac{k^2\left(n_1^2 - n_0^2\right)\cos^2\left(k_x a - \phi\right)\cos^2\left(k_y a - \psi\right)}{\left(1+\gamma_x a\right)\left(1+\gamma_y a\right)} \tag{1.19}$$

$$for \qquad \frac{n_0^2}{n_1^2} \approx 1$$

A demonstration of this approach can be exhibit at the analysis chapter 2.2.

1.3 Nanocrystal Background

Semiconductor nanocrystals offer exciting properties that are determined by their composition, size, and shape, allowing for bandgap engineering of their discrete electronic level structure and optical transitions. Research in this field is very active due to the great potential offered by these chemically synthesized nanocrystals. However, when one wants to build functional devices that utilize the enhanced nanocrystal properties, then the interaction of a large ensemble of nanocrystals is involved. To fully exploit the favorable nanocrystal properties, it is advisable to control and align all (or most) of the nanocrystals, so that their properties project towards the ensemble instead of averaging over all possible orientations. The properties of nanocrystals are governed by their bulk crystalline properties that are altered by their shape and physical confinement, which causes quantization of the energy levels while increasing the effective bandgap. Control over the size and shape of colloidal NCs is accomplished by simple control over the supply of precursors and thermal conditions during the chemical reactions that govern their growth. Further filtering procedure can be applied to narrow the NC's size distribution such that the optical activity matches the wavelength range of interest.

Due to size-controlled spectral tunability and chemical flexibility, semiconductor (SC) colloidal nanocrystals are very attractive for light-interacting applications, including fluorescent tagging [2], light-emitting diodes [3], and lasing [4]. The NCs show high photoluminescence, but limited gain properties due to low absorption cross-section [3], and fast nonradiative carrier recombination due to Auger recombination and abundance of surface states [5]. These shortcomings are dealt by surface passivation of the NCs using chemical ligands (called also "capping"), or growing an external "shell" made of different semiconductor material. The external interface can further serve to allow miscibility of NCs in different materials. The shell can also serve to alter the electronic levels by creating regular (or "Type I") electronic structure, where the electrons and holes are confined in the core, or "Type II" electronic structure, where the holes are confined in the shell. The latter configuration decreases the Auger recombination rate due to charge separation [6]. Growing NC in the shape of nanorods (NRs) is another way to decrease the Auger recombination rate while increasing the optical cross-section, and adding polarization dependence to its optical interactions [7, 8].

Figure 3 summarizes the bandgap size of different SC quantum dots (QDs). One can clearly see that some of the materials possess active properties in optical telecommunications wavelength of interest, i.e. InAs, PbS, PbSe, etc. Other NCs are interesting due to their permanent dipole moment (i.e., CdSe) which is amenable to external electric field orientation.

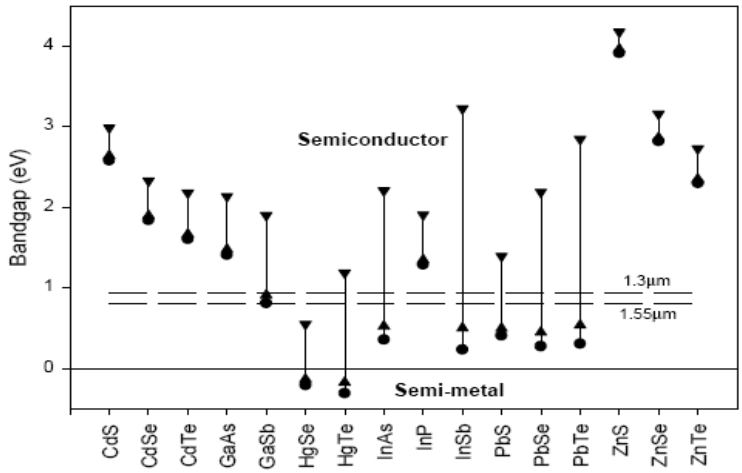

Figure 3: Sensitivity of bandgap energies to particle size for a range of semiconductors. Bandgaps are shown for the bulk forms (circles) and at dot radii of 10 nm (up triangles) and 3 nm (down triangles) [9].

1.4 Polymers Selection

Choosing polymeric material suitable for the common telecommunications wavelengths (800, 1300 and 1550nm) requires special care, as many molecular bonds have high absorption in the IR region due to resonances at these energies (especially the OH and CH bonds) [9, 11]. Flouropolymers are well suited for wave guiding IR light as they exhibit very low absorption (<0.15dB/cm) over the range of 400-1500nm, offer high temperature stability and long durability, can be patterned using standard spin coating, lithography and etching procedures, and have been combined with NCs to form a composite [12].

Our first goal is to adapt and further refine the techniques for dispersing QD and QR nanocrystals within the polymer host. Several approaches have been reported for incorporating nanocrystal quantum dots within polymers of various families for waveguide fabrication applications (PMMA [13], PFCB [12], and others). The process entails matching the nanocrystal to the polymer host, to ensure the miscibility of the QD into the host, and in some cases, protect the QD from a "hostile" environment. For example, Ref. [13] suggests a fast pre-polymerization of the nanocrystals to form oligomers that envelope the nanocrystal ('shelling'), which then allow for dispersal in a PMMA host. Ref. [12] suggests replacing the nanocrystal's native TOP/TOPO capping layer with an aromatic aniline capping ligand, to match the chemical structure of the caps to a PFCB host.
We will focus on NC alignment in Per-Flourinated Cyclo-Butane (PFCB) polymer, and compare it to the common Poly-Methyl Meth-Acrylate (PMMA) polymer.

For the cladding material we choose the Cytop™ polymer, a fluorinated polyether with refractive index of 1.34. This material exhibits excellent transparency over a wide range of wavelengths. Since the refractive index difference of Cytop™ and PMMA or PFCB is greater than 0.13 we expect a well confined optical mode. Figure 4 shows the transmission spectra of Cytop™ and PMMA films with thicknesses over 1.5 mm, and wavelengths between 350 to 1550 nm. When a PMMA/Cytop™/PMMA single mode waveguide is construct a 0.65 dB/cm propagation losses was measured at a 633 nm wavelength [14]. Figure 5 shows theoretical and measured attenuation of PFCB. As can be seen, PFCB exhibits sub-1-dB/cm clarity throughout the visible and

much of the near infrared. Measured losses for TVE-PFCB at selected wavelengths of interest are 0.17 dB/cm at 1310 nm, 0.39 dB/cm at 1490 nm, 0.29 dB/cm at 1550 nm and 0.60 dB/cm at 1590 nm [11].

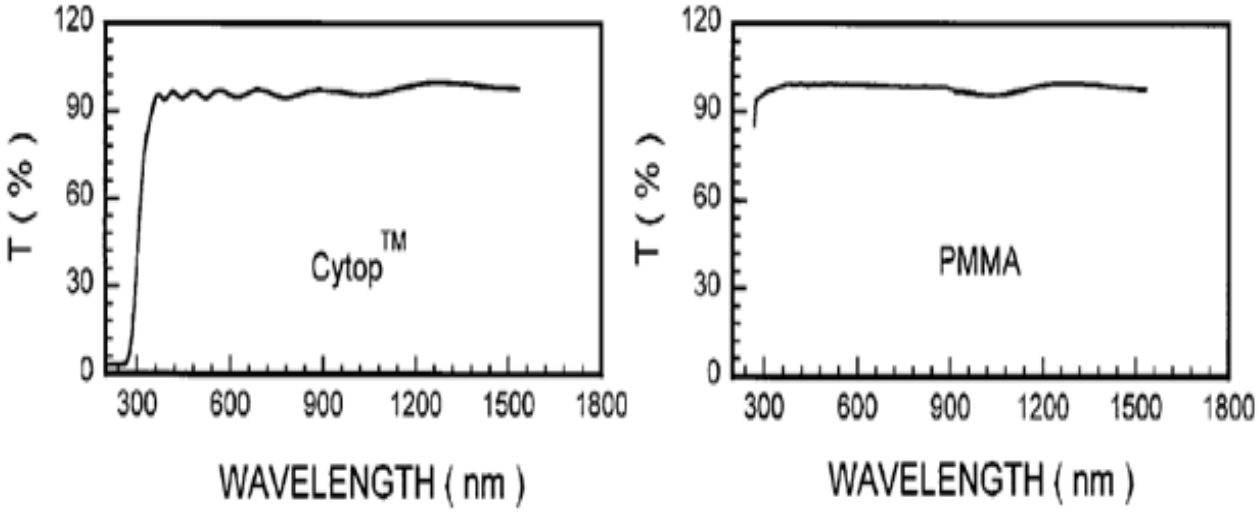

Figure 4: Room-temperature transmission spectra of the waveguide polymer components, Cytop™ and PMMA with thicknesses over 1.5 mm [14].

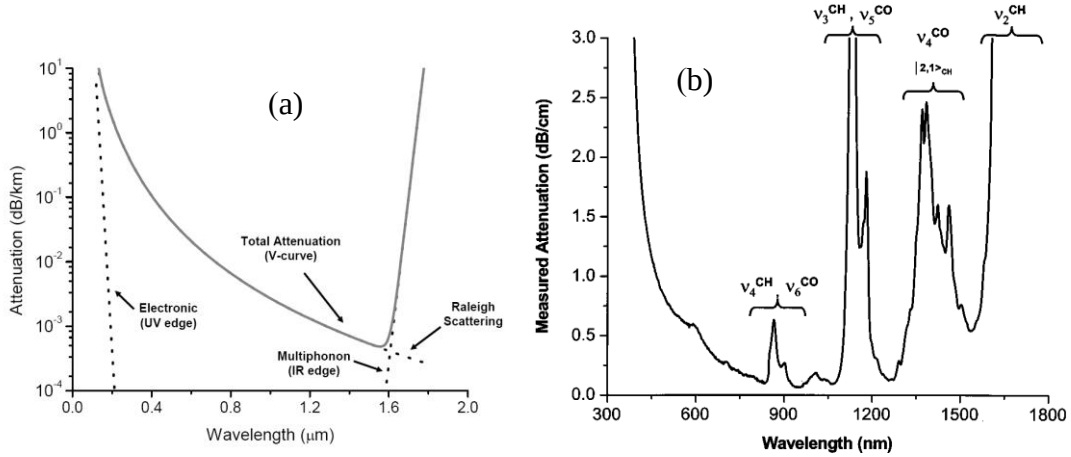

Figure 5: (a) Theoretical attenuation for PFCB calculated with computed electronic, multiphonon, and Rayleigh scattering spectral attenuation curves. (b) Measured attenuation versus wavelength for TVE PFCB. From [11].

Chapter 2

Waveguide and Device Design

2.1 General Assumptions

In this work we present Fabrication of waveguide from new materials that were never combined before to construct a highly confined waveguide mode. The refractive indices of the polymeric materials that we are using are Cytop n_0=1.34, PFCB n_1=1.47 or PMMA n_1=1.5 as cladding and core, respectively. The single mode requirement and the optical communication wavelength of 1550nm dictate the waveguides core dimensions. In Figure 6 the design dimensions are presented schematically.

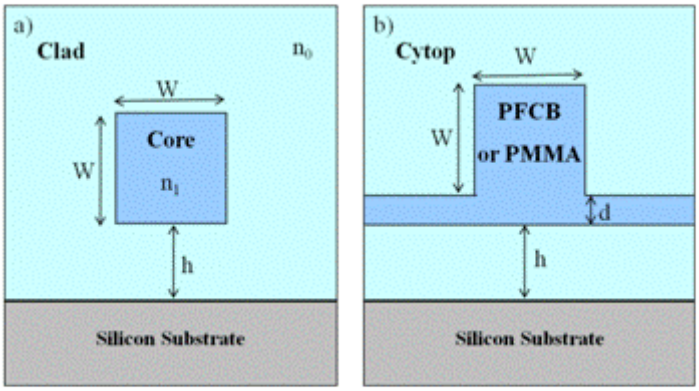

Figure 6: Waveguide design dimensions a) Square waveguide. b) Ridge waveguide

This chapter will present the analysis determining the desired devices and waveguide dimensions. We should note here that the final dimensions that are established in this analysis are the theoretical ones. The real dimensions analysis should include more variable such as walls roughness, bandwidth and fabrication constraints that are difficult to calculate. Therefore, the method is to fabricate various dimensions in the analytical region of interest and to acquire the best ones.

2.2 Waveguide Core Dimensions

Calculating the waveguide core dimensions requires a few numerical computation steps. In this analysis we use the Marcatili and the Kumar approximation (*section 1.1.2*) to obtain the *normalized* propagation constant in the core (Figure 7).

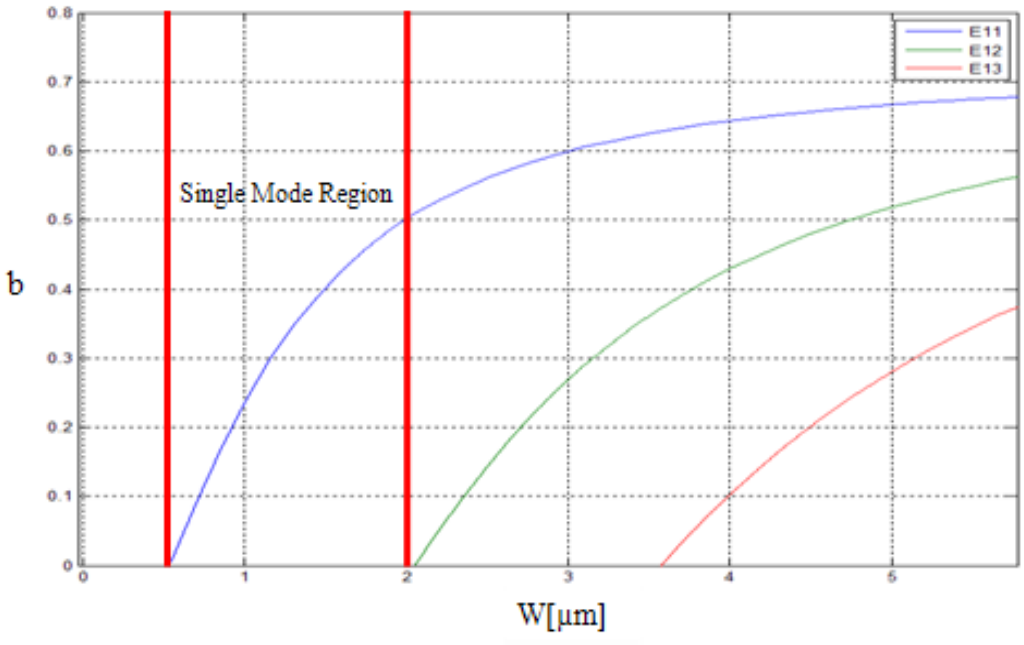

Figure 7: Normalized propagation constant graph Vs. WG width. With 1550nm wavelength for E^{y}_{11} E^{y}_{12} E^{y}_{13}

In order to obtain a single mode waveguide, it is necessary that the waveguide width will be small enough, to stay in fundamental mode, and no smaller than the cutoff width. For smaller wavelengths the second mode emerges at a smaller width of the core. On the other hand for larger wavelength the waveguide core can be bigger and

still obtain a single mode state. Since we would like to stay in the single mode region for a wide spectrum of wavelengths, the waveguide width is chosen to be 1500nm for 1550nm wavelength the calculated mode FWHM is 1.6 μm. In Figure 8 we can see the calculations for the ridged waveguide. The single mode state is still obtained.

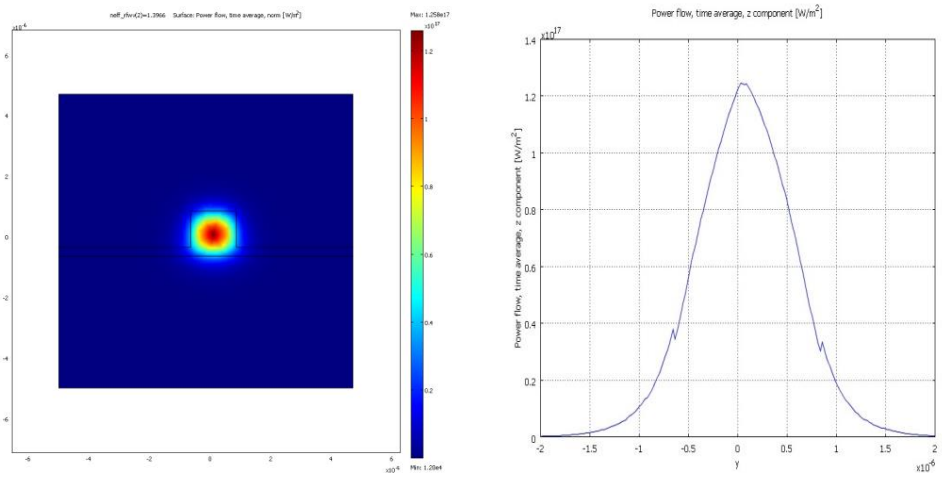

Figure 8**:** ridged waveguide mode calculation with a core size of 1.5μm.

2.3 Waveguide Clad Dimensions

Distancing the waveguide core from the silicon high refractive index substrate and from the Aluminum layer on the top is essential for preventing leakage of the optical power. This is done by calculating the electric field E^y and driving the optical intensity distribution in the cladding region. At the chosen distance of 4.5μm the calculated intensity is negligible for any loss. The intensity distribution can be seen at Figure 9.

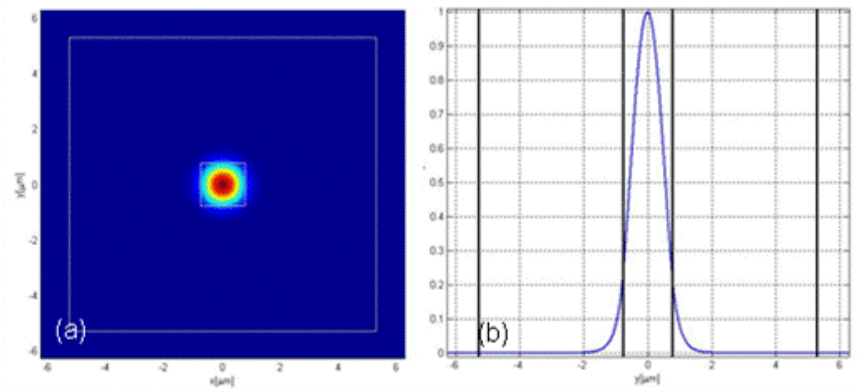

Figure 9: Intensity distribution

2.4 Waveguide Basic Characterizations

Since it is the first time that PFCB core and Cytop clad waveguide are combined, it is essential to provide the basic guiding characterizations. A great proportion of our lithography mask was designed for this assignment. The main two characterization features are the waveguide propagation losses and the bend losses.

2.4.1 Bend Losses

As we present a new platform of materials to construct an optical waveguide, the characterization of the waveguide bend loss is essential. The design of densely packed optical devices requires the knowledge of the involved bend loss and the ways to overcome them. The literature on curved guides contains a considerable variety of calculations and concepts, an early contribution being the 1969 paper by Marcatili [13] on curved slab and rectangular guides. An analysis by a conformal transformation, discussed in 1976 by Heilblum and Harris [16], represent the refractive index in polar coordinates and their transformation into Cartesian coordinate $x=R_t ln(r/R_t)$ is

$$\tilde{n}(x) = n(R_t e^{x/R_t}) e^{x/R_t} \tag{1.20}$$

Where R_t can be chosen arbitrarily. The transformed index profile is shown in Figure 10 for a curved slab guide with R_t equal to the radius of the outer wall. It indicates the exponential increase of the cladding index as the distance from the center of curvature increases [17].

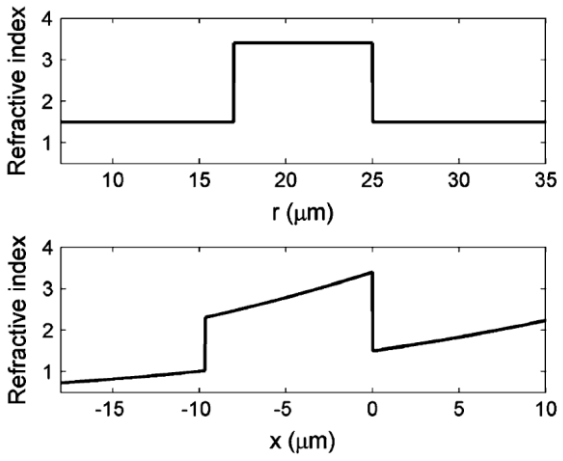

Figure 10: Transformed index profile of a slab guide with a tight bending radius at the outer wall of 25 μm [17].

A second effect is a shift of the mode power from the center of bend as a centrifugal force. Figure 11 shows a simulation for a bent fiber [18]. This shift, if not taken into account, can lead to a mismatch when the guided mode is coupled in to a straight waveguide or to a bends with a different curvature. To overcome this effect, the use of an offsets is suggested, to best match the mode patterns of coupled dissimilar guides.

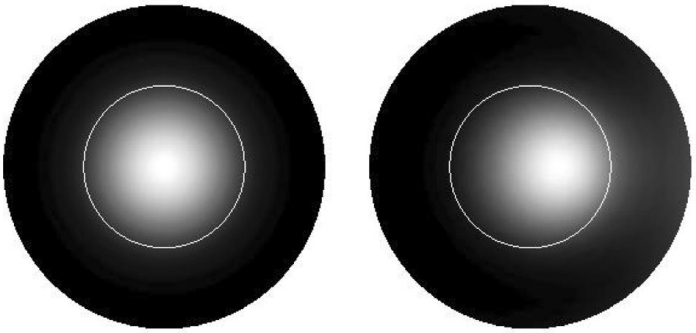

Figure 11: Outward shift of the modal field in a bent fiber for R = 1, left, and R = 1 cm, right. From [18].

In 1993 Dragone [19] suggested that for a small curvature bend the effective width w_0 has an effect on the fundamental guided mode. Numeric calculations were presented for a simple model, a planar waveguide formed by a curved strip of width w and a refractive index n, surrounded by index n-Δn. An optimization of the overlapping integral between the straight waveguide and the electric fields in the bend, determines the propagation constant

$$\varepsilon_{\infty} = \frac{2}{\sqrt{\frac{2\Delta n}{n}}} \exp\left[-\frac{3}{4}\left(Z^2 - 2.338 + b\right)^{3/2} \right] \qquad (1.21)$$

Where

$$Z = \left(\frac{2\Delta n}{n}\right)^{1/2} \left(\frac{k_0 R}{2}\right)^{1/3} \qquad b = \frac{1}{Z}\left(1 + \frac{0.65}{Z^2}\right) \qquad (1.22)$$

Figure 12 shows the calculation of the propagation constant of eq.(1.21) and for a beam propagation method both for 90º curvature. Both methods show that the losses are small for bends that are larger than 200μm. The beam propagation method was done for 15º curvature and then multiplied.

To characterize bend losses, an array of waveguides were designed, the array includes a varying number of 90º curvatures with different radii, all with core width of 2.5μm.

After each bend a taper narrowed the waveguide into a relaxation straight of the designated waveguide width of a 1.5μm. This was done to filter out higher order modes. The Lithography mask layout of Bend losses array is presented in Figure 12. Furthermore, a characterization of the bend loss can be provided by a ring resonator and will explain later.

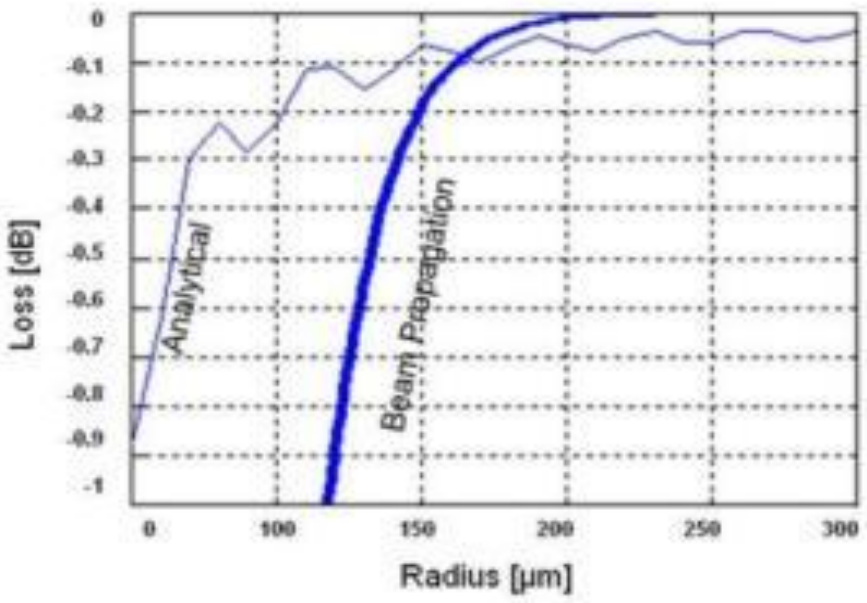

Figure 12: Bend losses vs. Radius graph with beam propagation method and analytical method.

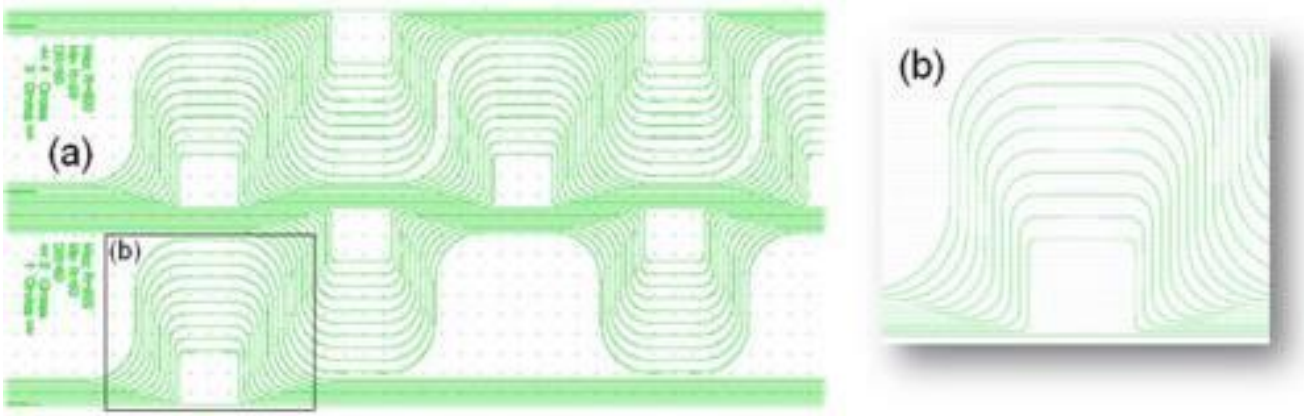

Figure 13: Lithography mask layout of Bend losses array.

2.4.2 Propagation Losses

Characterization of the waveguide propagation losses are done by designing an array of waveguides with different lengths. The waveguides designed as "S" shape with 90^{o} bend radiuses of 350µm. Figure 14 shows the Lithography mask layout. From previous works on Cytop core waveguides and PFCB core waveguides the expected Propagation Losses are ~0.15dB/cm [9-11]. For PMMA core waveguide we expect Propagation Losses of 0.65dB/cm [14].

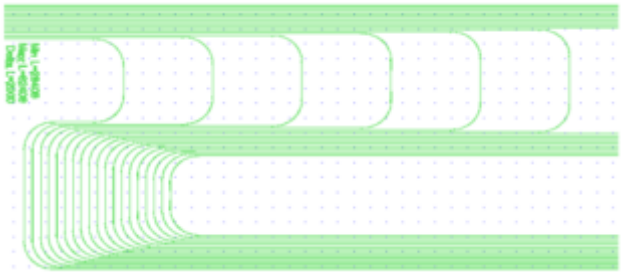

Figure 14: Lithography mask layout of propagation losses array

2.5 Device Dimensions Calculations

The use of materials that were never combined to form optical waveguide required some presentation of the new platform with known basic devices. Furthermore, our first motivation in fabricating this highly confined waveguide was to dope the core with semiconductor nanocrystals. These nanocrystals have some effect on the core refractive index [20]. To obtain the changes that will occur we designed devices that are sensitive to the refractive index such as ring resonators, directional couplers, multimode interference (*MMI*) waveguide and waveguide arrays star- couplers and *Mach-Zehnder* interferometers. The latter was designed for research of induced electrical or thermal fields on the arms. A star-coupler was designed just for fun.

2.5.1 Directional Coupler

Both analytical and beam propagation methods were used to design the directional coupler. We chose to construct -3dB coupler for 1550nm wavelength. The directional coupler is shown schematically in Figure 15 and Figure 16. The final dimensions are: coupler length L=70µm, the distances between the waveguides centers is D=2.5µm for the -3dB coupler. To achieve this an array of couplers were designed with a D of

1.6 to 3.5μm. The curves are 15° with 350μm radius to avoid bend losses as discussed in the previous subchapter.

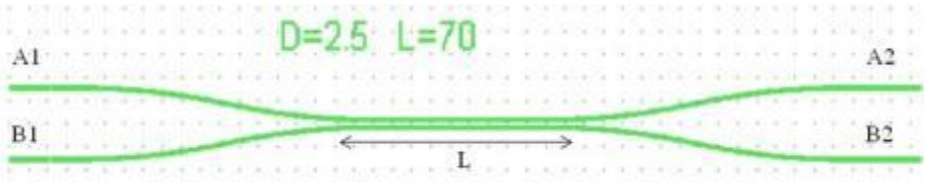

Figure 15: Lithography mask layout of directional coupler

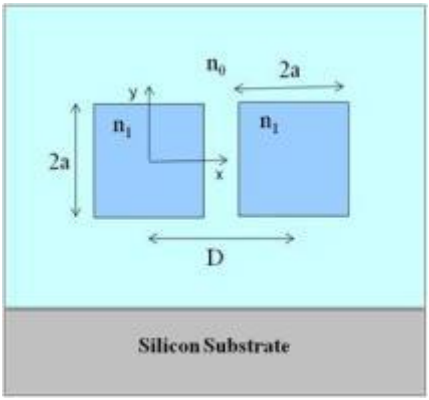

Figure 16: Directional coupler design dimensions

Analytically [1], the coupling coefficient κ is given by

$$\kappa = \frac{\sqrt{2\Delta}}{a}\frac{(\kappa_x a)^2(\gamma_x a)^2}{(1+\gamma_x a)v^3}\exp[-\gamma_x (D-2a)] \qquad (2.1)$$

Parameters κ_x, κ_y and γ_x, γ_y are obtained by solving the eigenvalue problem. By using the coupler field transition Equation (2.1) we can calculate the desired coupling length (L). To construct a -3dB coupler with $\kappa L=\pi/4$ light-splitting regions are $A_2=A_o/\sqrt{2}$ $B_2=-i\,A_o/\sqrt{2}$.

$$A_2=A_o\cos(\kappa L) \quad B_2=-jA_o\sin(\kappa L) \qquad (2.2)$$

It should be noted that the mode coupling takes place not only in the straight coupling region but also in the curved regions. Therefore the coupling length L is an effective straight coupling. Fabricated final structures have some variations from the initial lithography mask design. To overcome this problem, an array of directional couplers was designed on the lithography mask with different distances between the waveguides centers. In Figure 17 shows the calculation the coupler's required length

for κL=π/4, as a function of the wavelength and D=2.5[μm]. It can be seen that for the mean of TE and the TM modes the coupler length is about 70μm at λ=1550nm. The intensity ratio between the arms is very sensitive to variations of the distances between the waveguide centers, as seen in Figure 18. Figure 19 demonstrates the sensitivity of the coupler to the increase in the refractive index that will take place after doping with nanocrystals.

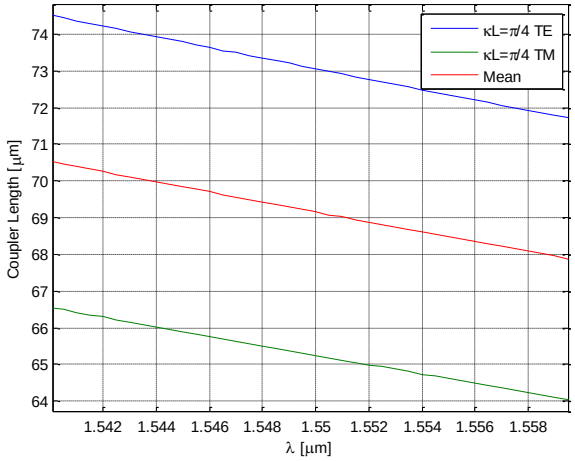

Figure 17: Directional Coupler Length to wavelength for κL=π/4 and D=2.5[μm].

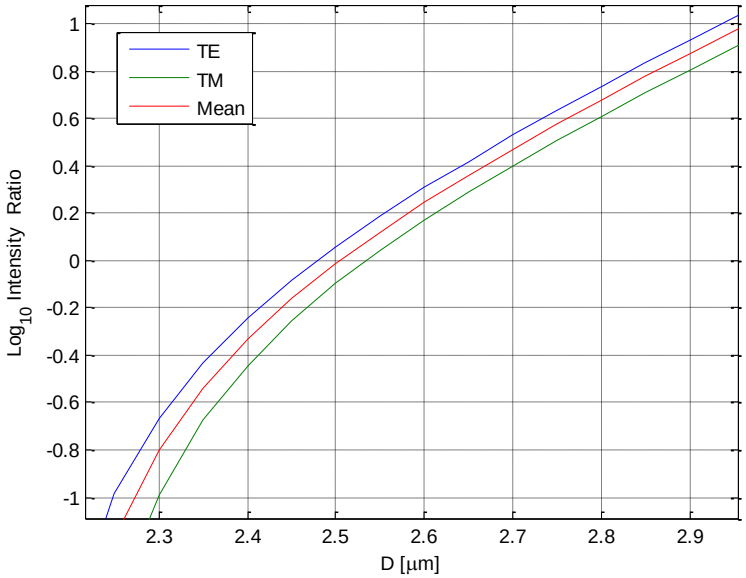

Figure 18: Directional Coupler Intensity Ratio between arms to distances between the waveguides centers L=70[μm] λ=1550[nm].

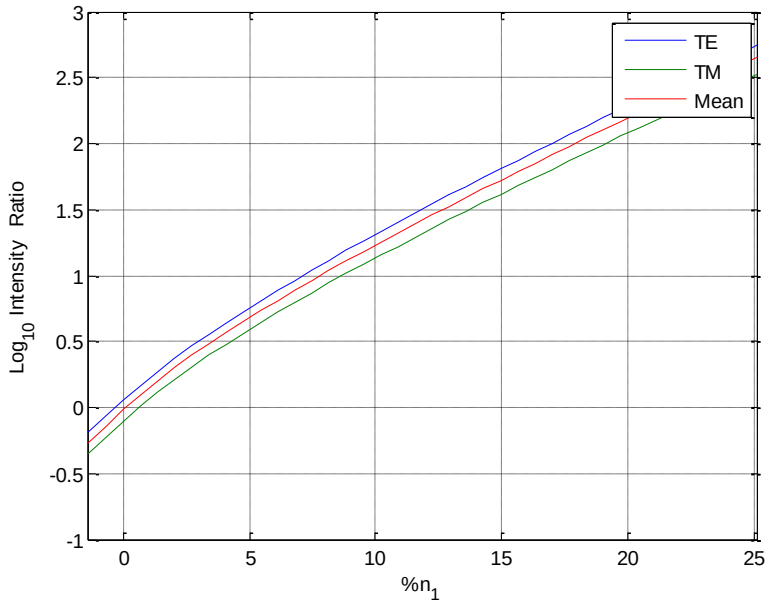

Figure 19: Directional coupler intensity ratio between arms to percentage of change from refractive index of PFCB L=70[μm] D=2.5[μm] λ=1550[nm].

2.5.2 Multimode Interference Coupler

Multimode Interference Coupler (MMI) has been design again with an analytical and beam propagation method. The dimensions that should be calculated are illustrated in Figure 20. We choose to construct -3dB coupler for 1550nm wavelength again. The absence of the small separation region between the coupled waveguides makes the MMI device easier to fabricate then the directional coupler.

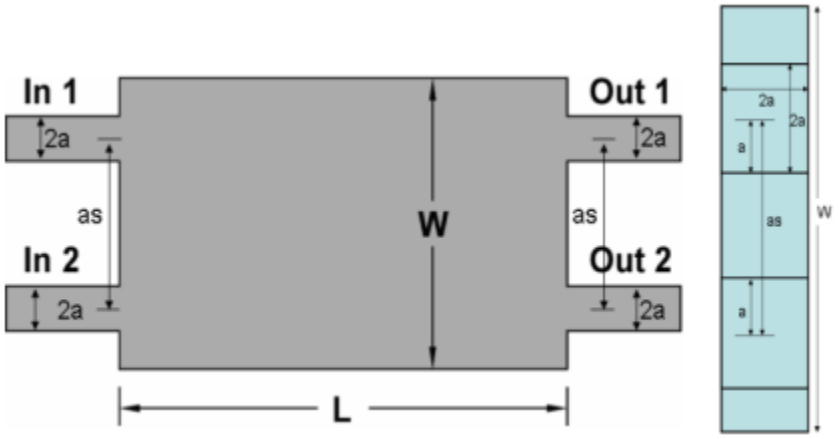

Figure 20: Multimode Interference coupler dimensions

A few general assumption were in order, the device should work properly in 1.3-1.6μm wavelength, a minimum polarization dependence (PDL), a short as possible

device with maximum intensity as possible , symmetrical output and input and single mode input and output. To get maximum power at the output it is necessary to have more then three modes in the MMI region. By choosing the input output positions it is possible to cancel unneeded modes [21]. The MMI width was chosen to hold four modes. Again length *L* is an effective straight coupling and the curved regions are neglected from the analytical calculations.

Parameters κ_x, κ_y for all modes are obtained by solving the eigenvalue equations (1.8). The one dimensional fields distributions are calculated by (1.5) and multiplied to form the two dimensional fields. The single mode input field is admitted to the MMI by the following overlapping integral

$$\eta_{pq} = \frac{\int_{-\infty}^{\infty}\int_{-\infty}^{\infty} \varphi(x,y)\phi_{pq}^{*}(x,y)dxdy}{\sqrt{\int_{\infty}^{-\infty}\int_{\infty}^{-\infty} \varphi(x,y)\varphi^{*}(x,y)dxdy}\sqrt{\int_{\infty}^{-\infty}\int_{\infty}^{-\infty} \phi_{pq}(x,y)\phi_{pq}^{*}(x,y)dxdy}} \tag{2.3}$$

The field in the MMI is calculated by

$$E(x,y,z) = \sum_{pq} \eta_{pq}\phi_{pqi}(x,y)e^{i\beta_{pq}\cdot z} \tag{2.4}$$

The output field can then by derive by

$$\eta_{1/2} = \frac{\int_{-\infty}^{\infty}\int_{-\infty}^{\infty} E(x,y,L)\varphi^{*}(x\pm as,y)dxdy}{\sqrt{\int_{\infty}^{-\infty}\int_{\infty}^{-\infty} \varphi(x\pm as,y)\varphi^{*}(x\pm as,y)dxdy}\sqrt{\int_{\infty}^{-\infty}\int_{\infty}^{-\infty} E(x,y,L)E^{*}(x,y,L)dxdy}} \tag{2.5}$$

Finally the output power can be calculated

$$P_{1/2} = \underbrace{\frac{1}{2}}_{for\ Ex\ and\ Ey} \sum_{pq} \eta^{2}{}_{pq} \int_{-\infty}^{\infty}\left(\sum_{i} \eta_{1/2}\phi(x)\right)^{2} dx \tag{2.6}$$

Figure 21 shows the power distribution within the MMI device. In Figure 22 (b) we can see the outputs power ratio as a function of the MMI length and in Figure 22 (a) we can see the total output power for both outputs as a function of the MMI length. As expected the total power is oscillating along the L direction. The power cycles in

the MMI as in a multimode waveguide and demonstrated in(2.7) for Power distribution in a four mode waveguide, due to the different modal propagation parameter, β.

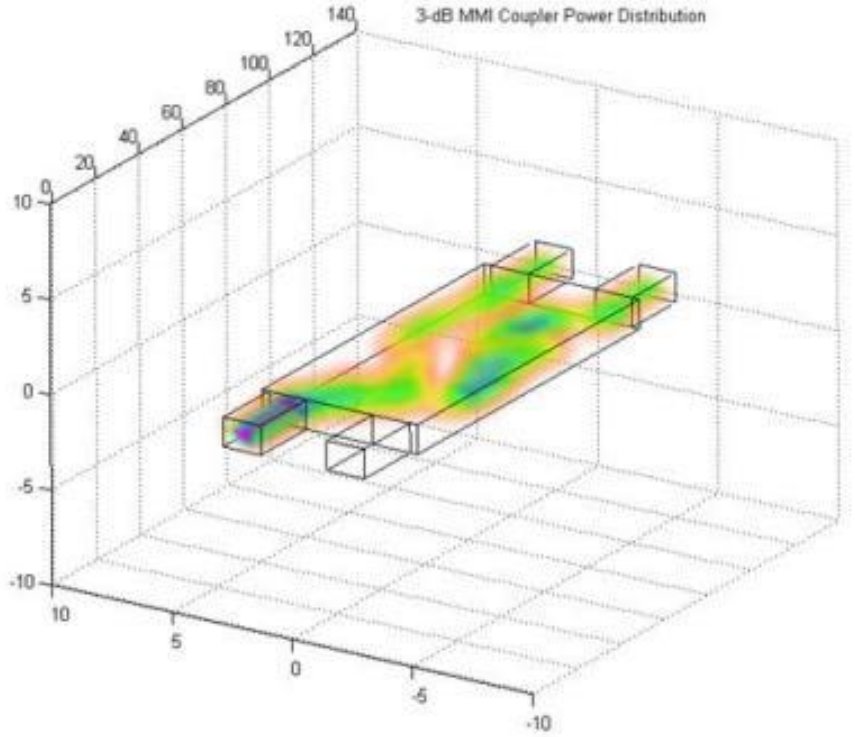

Figure 21: MMI power distribution

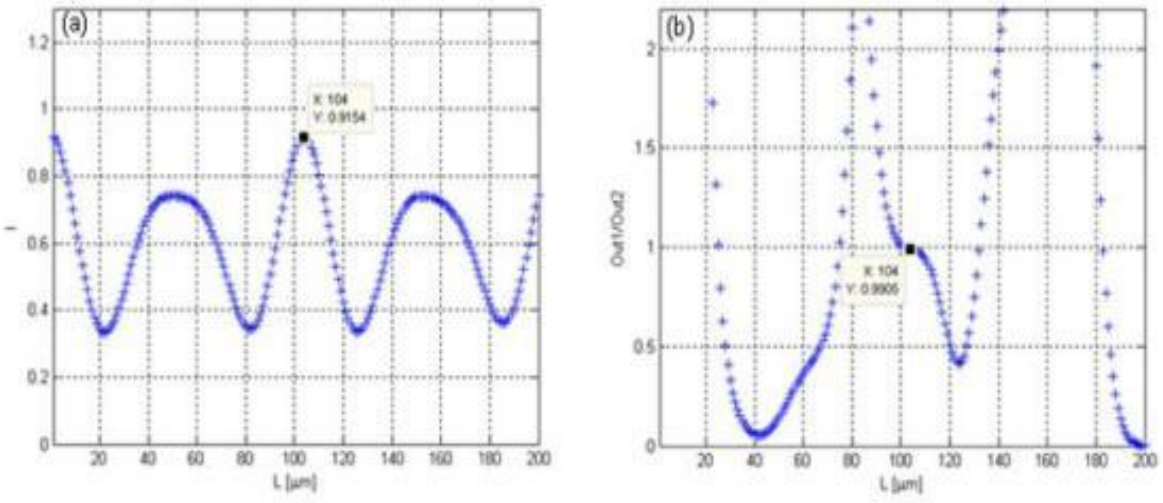

Figure 22: (a) Sum of the total power at both outputs to MMI length, maximum power will be at a length of 104µm. (b) Outputs power ratio to MMI length, a length of 104µm is needed for the -3dB coupler**.**

$$P = \int_{-\infty}^{\infty}\int_{-\infty}^{\infty}(E_{11}e^{i\beta_{11}L} + E_{12}e^{i\beta_{12}L} + E_{13}e^{i\beta_{13}L} + E_{14}e^{i\beta_{14}L})\cdot(E_{11}e^{-i\beta_{11}L} + E_{12}e^{-i\beta_{12}L} + E_{13}e^{-i\beta_{13}L} + E_{14}e^{-i\beta_{14}L})dxdy =$$

$$= \int_{-\infty}^{\infty}\int_{-\infty}^{\infty}\sum_{k}^{4}E_{1k}^2 + (E_{11}E_{12}(e^{i\Delta\beta_{1112}L} + e^{-i\Delta\beta_{1112}L}) + E_{11}E_{13}(e^{i\Delta\beta_{1113}L} + e^{-i\Delta\beta_{1113}L}) + ... + E_{12}E_{13}(e^{i\Delta\beta_{1213}L} + e^{-i\Delta\beta_{1213}L}) + ...)dxdy = \quad (2.7)$$

$$= \sum_{k}^{4}p_{1k}^2 + p_{1112}\cos(\Delta\beta_{1112}L) + p_{1113}\cos(\Delta\beta_{1113}L) + ... + p_{1213}\cos(\Delta\beta_{1213}L)... \approx A + B\cos(\Delta\beta_{1112}L) *$$

Here too an array of MMI were designed to get the required -3dB coupler. The curves are 15° with 350μm radius the Lithography mask layout of a MMI coupler is presented at Figure 23. The final dimensions that were selected *W*=6.5μm, *L*=10-120μm, *as*=4.3μm and *2a*=1.5μm. Analysis with beam propagation method was preformed as well and the results are very close to the analytical ones.

Figure 23: Lithography mask layout of a MMI coupler

2.5.3 Racetrack Resonator

Racetrack resonators are a standard planer waveguide device with a very straight forward dependency on the refractive index. Furthermore, the bend losses of the specific radius can be extracted as well. The device is shown schematically in Figure 24. The basic analysis of the exchange of optical power between the waveguide and a resonator were given by Yariv at 1997 [25].

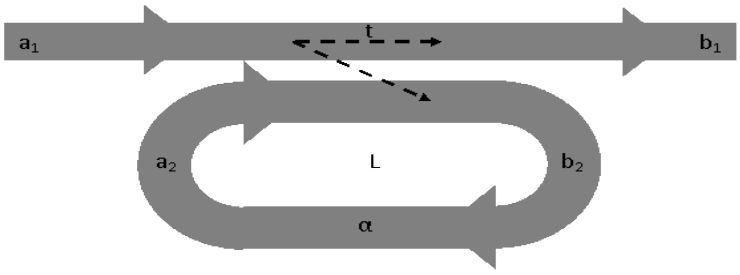

Figure 24: Racetrack resonator

The output and input functions are given by

$$\begin{aligned} b_1 &= t \cdot a_1 + \kappa \cdot a_2 \qquad |t|^2 + |\kappa|^2 = 1 \\ b_2 &= k^* \cdot a_1 - t^* \cdot a_2 \qquad a_2 = b_2 \alpha e^{i\theta} \end{aligned} \tag{2.8}$$

Then the transfer function will be

$$T = \frac{|b_1|^2}{|a_1|^2} = \frac{\alpha^2 + |t|^2 - 2\alpha|t|\cos\theta}{1 + \alpha^2|t|^2 - 2\alpha|t|\cos\theta} \tag{2.9}$$

$$\theta = \frac{2\pi L n_{eff}}{\lambda} \qquad \alpha = e^{\frac{-\alpha_T L}{2}} \tag{2.10}$$

Where L is the total racetrack length and α_T is an "*absorption loss coefficient*" $\left[cm^{-1}\right]$. We obtain the resonance wavelength peaks spacing as

$$\Delta\lambda = \frac{\lambda^2}{n_{eff} L} \tag{2.11}$$

In Figure 25 we demonstrate the calculated transition function for a 350μm Radius with a 100μm coupling region α=0.67 t=0.637 n_{eff} was calculated for 1550nm wavelength with a 1.47 refractive index for a PFCB core and for the NC doped core with a 1.48 refractive index.

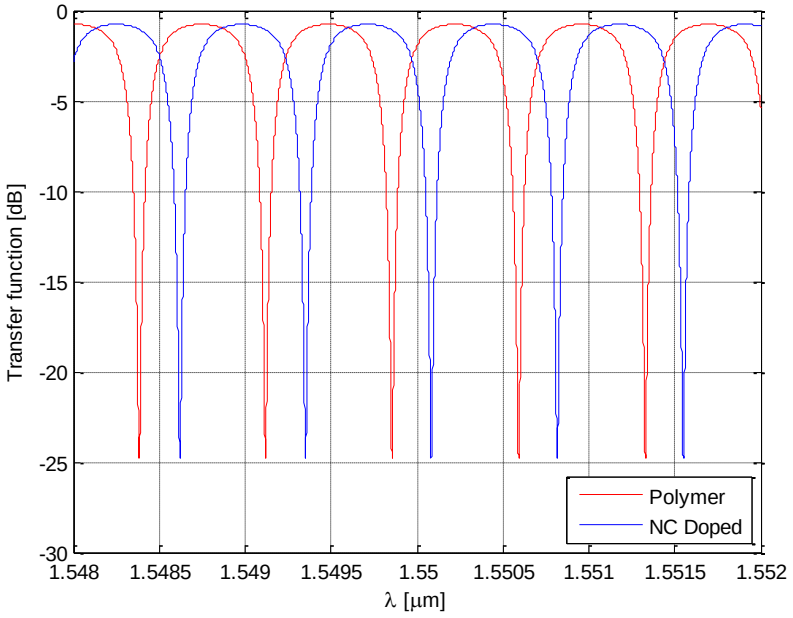

Figure 25: Racetrack resonator transition function

Our racetrack resonator is based on the same assumptions as for the directional coupler as the coupling region is same as for a directional coupler. An array of racetrack resonator with different radii and directional coupler spacing were designed. Figure 26 shows the Lithography mask layout.

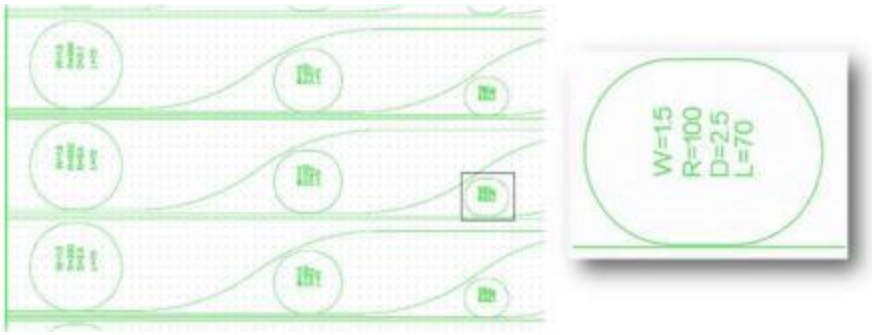

Figure 26: Lithography mask layout of racetrack resonators.

2.5.4 Waveguide Array

Nonlinear waveguide array can be used for parallel information processing. We will use them as another test for coupling efficiency and for observing changes in the refractive index after nanocrystals doping. Figure 27 presents a beam propagation analysis of a waveguide array, here the light is imposed in to the array at the middle and the intensity is analyzed on the fifth output waveguide for variation of refractive indexes. A variation of waveguide arrays were designed with different coupling distances and width.

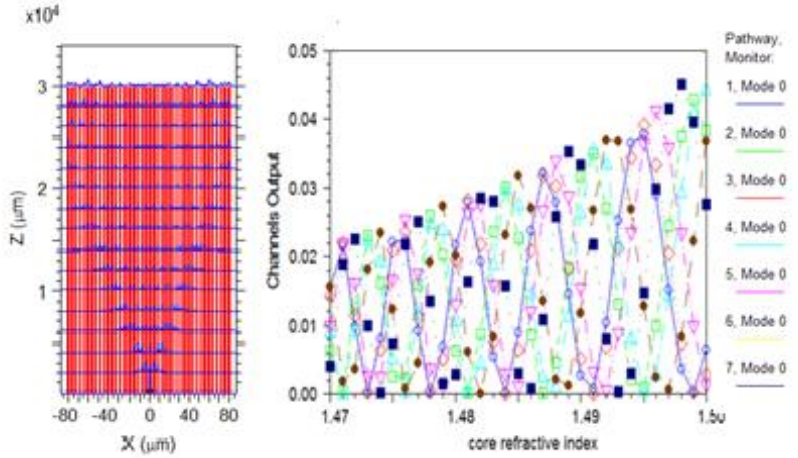

Figure 27: waveguide array analysis

2.6 External Coupling

Coupling light in to an optical waveguide requires the precise alignment of a light beam upon the waveguide input. To achieve the best coupling as possible the applied beam lateral distribution should match the desired optical mode distribution in the waveguide. Commercial lensed fiber (Figure 28) can provide a beam spot size of 2.5µm, since our waveguide core dimensions are 1.5µm we need the use a taper. To get best coupling efficiencies and mode matching abilities in a taper it is necessary to design a taper that will insert the required mode in to the optical waveguide device. By designing a moderate slope taper it is possible to avoid neighboring modes [26].for 2.5µm single mode spot size the taper dimensions should be 3µm. To avoid neighboring modes the taper length is 150µm. We should note that the taper can be designed only in the planer dimensions for fabrication reasons. Figure 29 demonstrates a lensed fiber coupling light in to a taper.

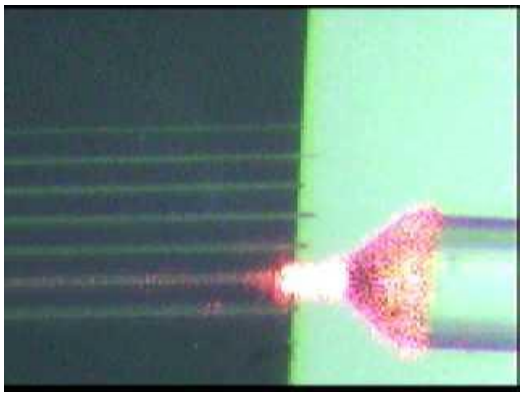

Figure 28: Commercial lensed fiber

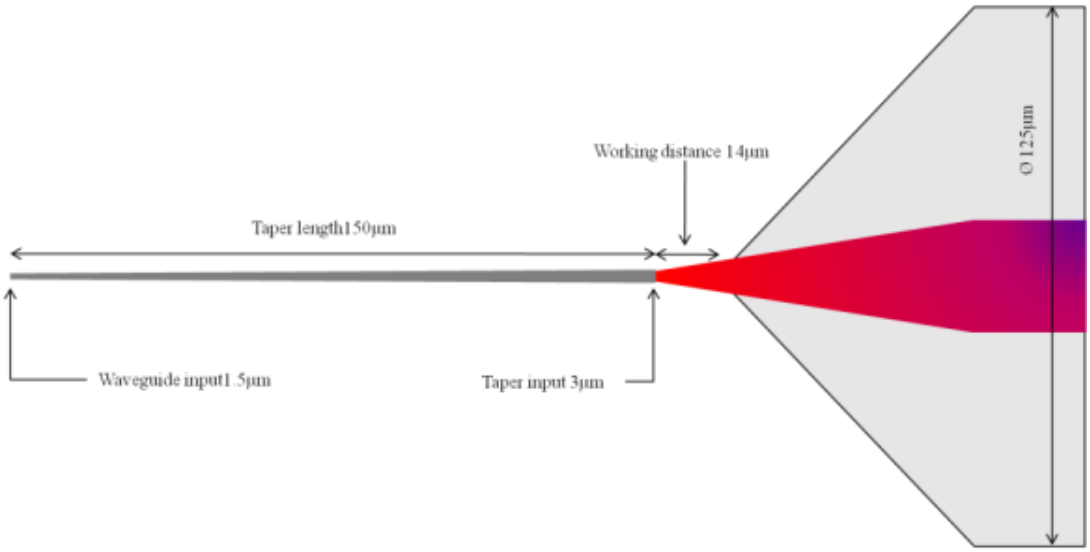

Figure 29: lensed fiber coupling light in to a Taper

Chapter 3

Waveguide Fabrication

3.1 General Description

The main objective of this work is the process development and fabrication of a waveguide structures with a PFCB polymer core and Cytop polymer as cladding. The device structure is shown schematically in Figure 30. At first buried waveguide geometry were fabricated (a) but in order to overcome structural movements a ridge waveguide design was formed (b).

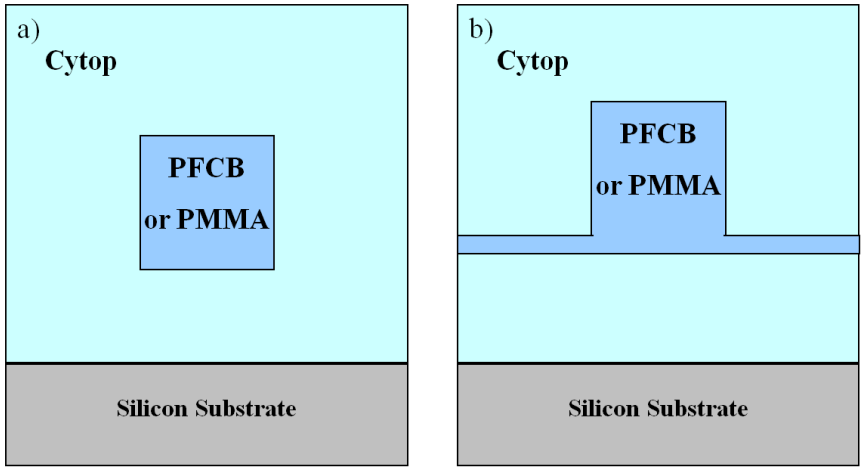

Figure 30: Device structure a) Square waveguide. b) Ridge waveguide.

PBCB is synthesized from two polymer powders, trifluorovinyl aromatic ether (TVE) and biphenylperfluorocyclobutyl (BP). Synthesizing the PFCB is a long, difficult process, and yields a small amount of material. Therefore most of the process development was done with a commercial PMMA polymer core, as it is a more standard and cheaper material that has the same physical and some of the optical characteristic [14] of PFCB. PMMA can provide a nanocrystal matrix as well [13]. Previous work has been done with PMMA core and Cytop cladding [14].

Since most of the fabrication tools that were used are from the semiconductor field such as the lithography mask aligner, spin coaters and more, a simple 2'' single sided polished silicon wafer was chosen as the substrate. Moreover, combining optical devices in integrated circuit will be possible for future applications.

The process development was a long and difficult stage of this work. A few process flows were suggested until the final process was established. The main difficulty of the fabrication process is to maintain low defect tolerance for long and small WG up to 2 cm and with a width of 1.5μm. This low defect tolerance had contributed for canceling some process ideas such as liftoff lithography. In the following chapter the process steps and the solutions to the difficulties that occurred will by explained.

It should be noted here that after most of the process development was done the unit of nanofabrication (UNF) obtained a new reactive ion etch (RIE) system, that is also a plasma enhanced chemical vapor deposition (PECVD), that is equipped with a cooling system that is specialized for depositing materials on polymers. The outcome process of this system will be described in chapter 3.2.2. PECVD or flame hydrolysis processes usually occurs at high temperature, after the wafer has cooled, stress can build up within the silica and between the silica and the silicon substrate. The stress arises both from a mismatch in the coefficient of thermal expansion (CTE) and from a contraction of the silica film as it is sintered. Without the cooling system, the stress produces a defective silica layer.

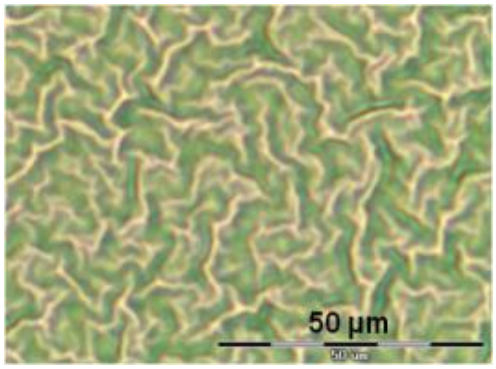

Figure 31: microscope image of a typical defected silica layer over Cytop

3.2 Process Development

3.2.1 PMMA Core Waveguide

Step 1 – Cytop Adhesion to Silicon

Cytop A grade has poor adhesion to silicon. It is impossible to spin coat a thin film of Cytop on a silicon substrate. Therefore, a substrate preparation for the Cytop is needed. Cytop has good adhesion to metals such as aluminum, silver and iron and for Plastics such as PMMA. A Silane coupling agent can be used as well.

Due to these characteristics, a simple thin Aluminum layer was suggested for its future possibility to act as an electrode. A 0.5µm Aluminum layer was evaporated on the wafer. After spin coating and curing of the Cytop, small 1µm round black defects were observed (Figure 32), therefore Aluminum as an adhesion layer was abandoned.

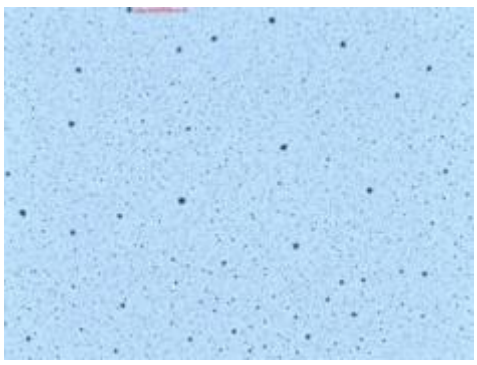

Figure 32: ~1um round black defects on Aluminum layer after Cytop deposition.

A thin 200nm PMMA A2 (2% Solids in Anisole) layer deposited by spin coating was suggested due to its simplicity. Process development went on with this adhesion promoter until it was determined that multi layering of polymers have high defect likelihood and it is better to avoid if possible. Silane coupling agent was tested, and after a few experiments the process was stabilized.

Step 2 – Cytop Under-Clad Spin Coating

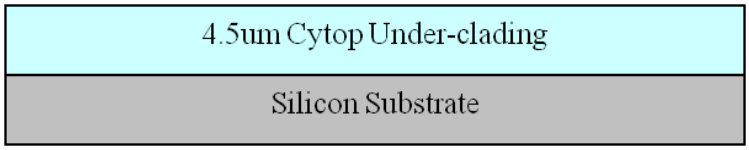

A 4.5um thick under-clad layer of Cytop was needed in order to establish a far enough waveguide core from the high refractive index of the silicon substrate. The manufacturer datasheet suggested multi layering of 2um layers. As before, multi layering of polymers is not favorable for its defect stacking. A low velocity spin coating was chosen. This slow spin leave small rumples in the middle of the wafer but they disappear after the curing process of the Cytop. When a simple curing step of 180^{o}C is applied, defects occur all over the wafer. It is essential to conduct the curing process in a few ramping steps to get a homogeneous layer.

Step 3 – PFCB\PMMA Adhesion to Cytop

Cytop is an amorphous fluorocarbon polymer and as such it is hydrophobic Teflon-like film. A short O_2 plasma etching surface treatment is needed for opening some Surface bonds. This process is necessary to help the next PMMA spin coating adhesion to succeed.

Step 4 –PMMA Core Spin Coating

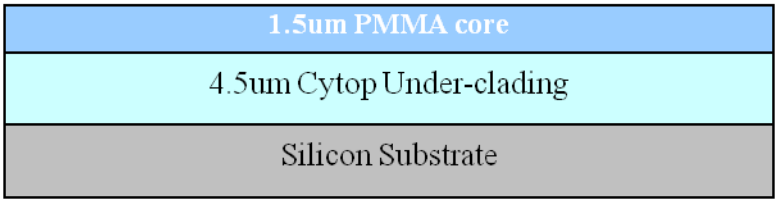

The PMMA is spin coated and cured on a hotplate for a minute and a half.

Step 5 – Cytop Over-cladding Spin Coating

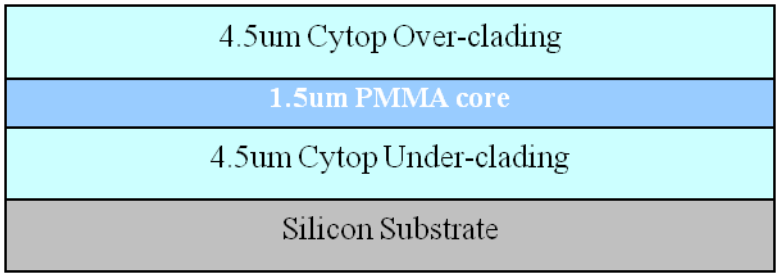

A 4.5um thick over-clad layer of Cytop was needed again, this time to distance the waveguide core from the metallic hard mask that will be evaporated in the next step. Again, a slow spin coat and curing process of a few ramping step is needed for Homogeneous layer.

Step 6 – 100nm Aluminum

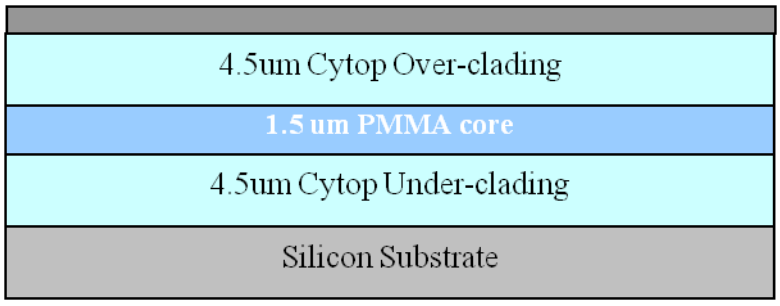

In the process of etching the waveguide channels by reactive ion etching (RIE), it is necessary to provide a mask material that has different sensitivity for the etching chemistry (Selectivity), this element is referred to as a hard mask. Since the photoresist is also an organic polymer, the etching rate of Cytop and the PR are roughly the same. It is impossible to get the wanted aspect ratio with the use of a PR mask at the RIE process.

When depositing the hard mask, several difficulties can occur in the form of cracks, thermal expansion mismatch of the polymer, and adhesion problems of the hard mask to the Cytop over cladding.

First approach was a metal mask, since Cytop has no adhesion problems to metals. First we tried a 10nm Chromium mask. Unfortunately it wasn't thick enough to stand the RIE process, the results can by seen at Figure 33. Thicker layers of 20nm-100nm Chromium were tested, but when heated to the 110^{o}C that is needed for the prebake of the photoresist in the next lithography step, the chromium cracked immediately, a typical result can by seen in Figure 34.

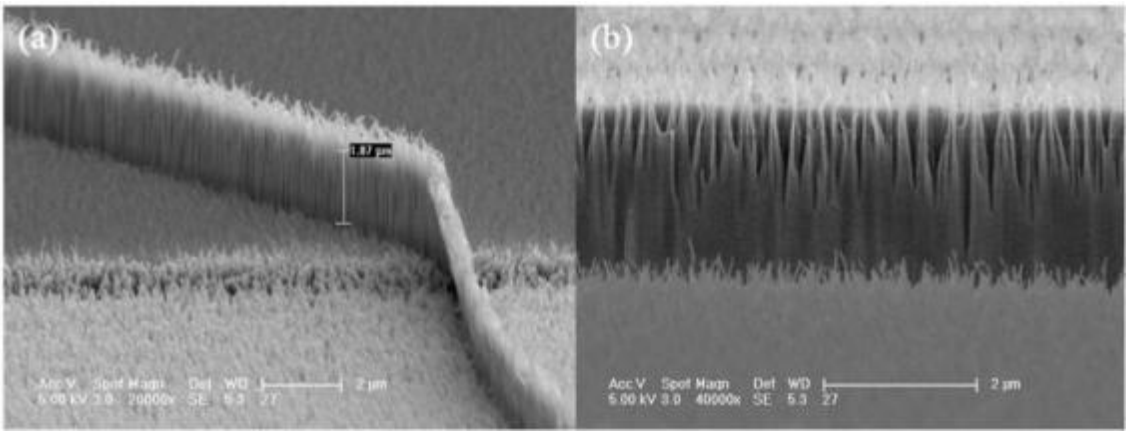

Figure 33: SEM Image of waveguide after RIE process with a 10nm Cr mask (a) General view. (b) Side view.

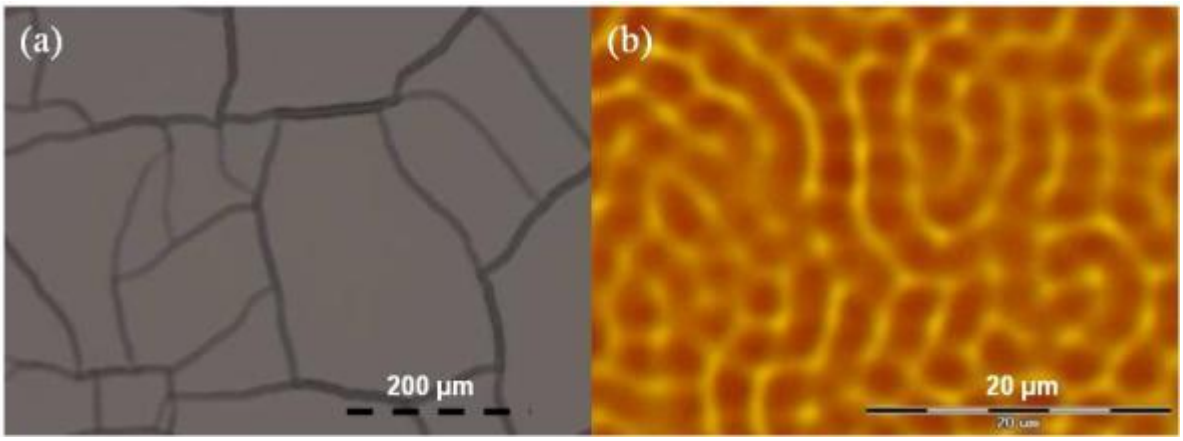

Figure 34: (a) Microscope Image of 20nm Cr layer on Cytop after curing. (b) Typical defect Aluminum layer over Cytop after 1 minute 100^{o}C hotplate back.

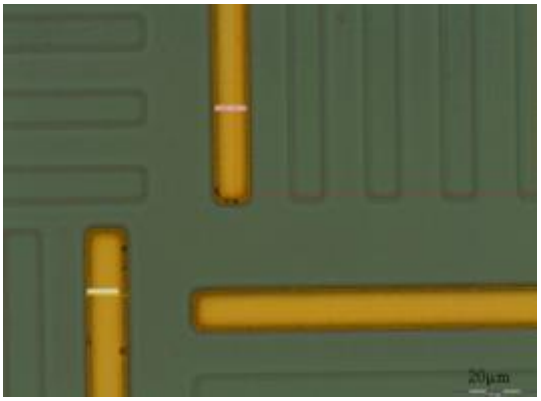

Figure 35: Damaged waveguides after liftoff lithography

A set of experiments was conducted with a Titanium, Ti\Au, Cr\Au and Aluminum by evaporation, all samples cracked. Liftoff lithography was suggested since there is no need of heating the metallic layer after evaporation. Unfortunately liftoff in such a small scale and small defect tolerance is problematic, and didn't achieve the desired quality and reliability (Figure 35)**.**

Previous work suggested overcoming these problems by a 100nm thick Aluminum evaporated layer on the Cytop over clad and a 90ºC curing step on a hotplate for 10 minutes for the prebake of the photoresist [27]. This method proved successful.

Second approach was to sputter a layer of silica. This was possible just after obtaining the cool PE-CVD process. Since most of our work was done without this system we will describe the new process at chapter 3.2.2.

Step 7 – Lithography – PR Spin-coat, Prebake, Exposure, Post-bake, Develop

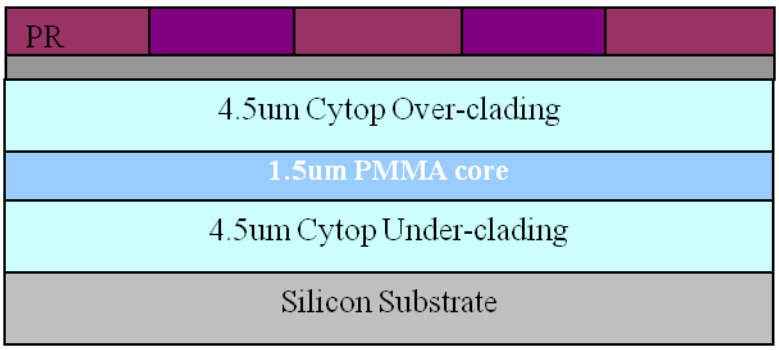

Lithography is a stable and standard process step. Elements that are Smaller that 1um are still hard to achieve. In our design, we attempt to get to this size regime. This is

possible thanks to new SUSS mask aligner that was purchased by our group. A 0.5um thin layer of AZ1505 photoresist layer was needed to achieve the small resolution elements. The prebake and the post bake were changed from standard, in order to protect the Aluminum layer as discussed in the last step. A short expose time is needed as the Aluminum layer is a refractive layer in the UV wavelength and for the thin photoresist layer. Developing was done in the standard way.

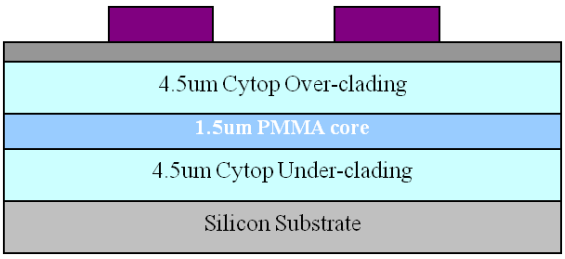

Step 8 – Aluminum wet etch

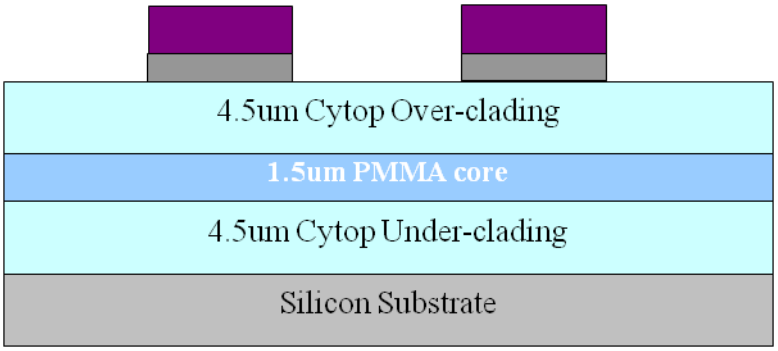

A standard Aluminum wet etch solution made of Phosphoric Acid (H_3PO_4)(w/w) 72.5-74.5%, Nitric Acid (HNO_3)(w/w) 1.7-2.3%, Acetic Acid (CH_3COOH)(w/w) 9.5-10.5% and Glycerin $C_3H_5(OH)_3$ 0.5%. The wafer was dipped in the solution; stop time is determined by a visual examination.

Step 9 – O_2 Reactive Ion Etching (RIE)

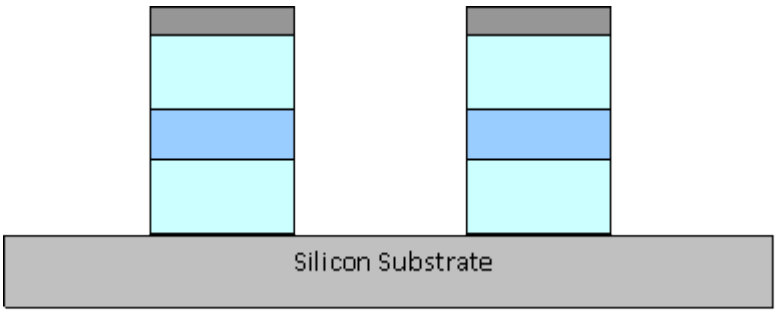

The RIE process was initially done at Tel-Aviv University nanofabrication unit with a Nextral 860 RIE/HDP plasma etcher machine. The process recipe is a standard O_2 resist removal. At first we wanted to etch just a little short than the waveguide core. Unfortunately that leaves strands like surface that can be seen in Figure 36. The absence of these strands near the waveguide channels is necessary to avoid optical losses from the waveguide core.

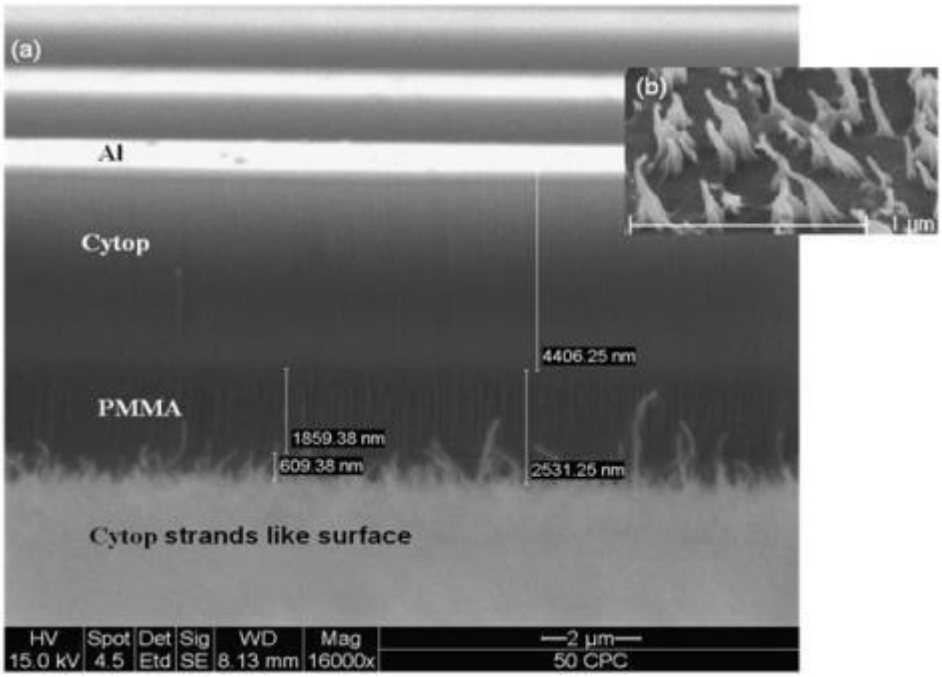

Figure 36: SEM Image of Cytop strands like surface after RIE process. (a) Side view. (b) Zoom on strands.

To avoid strands-like surface, the RIE process is set to etch all the way to the silicon Substrate (Figure 37). It is important that roughness of the waveguide side walls will be as small as possible for minimum optical losses. In this process the side walls roughness are in the 100nm scale Figure 38. It may by possible to smooth the roughness by dipping in solvent [29].

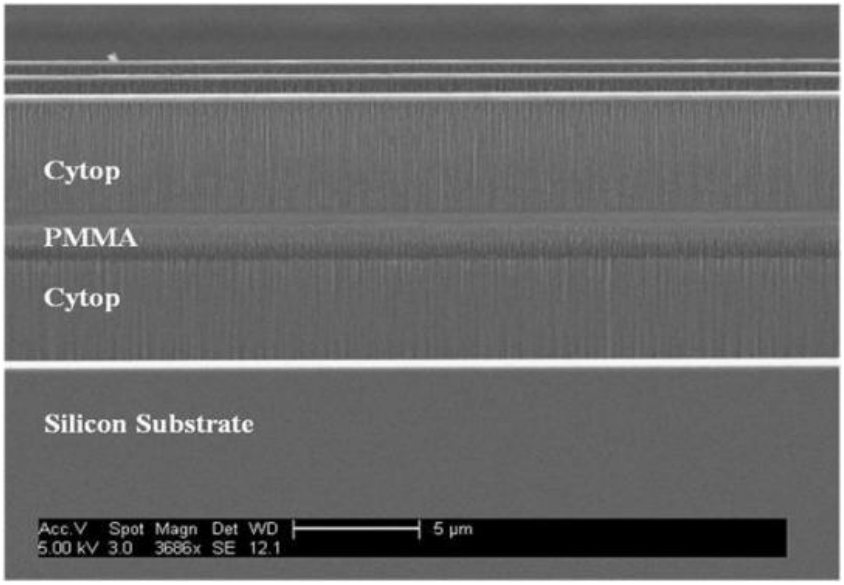

Figure 37: SEM Image WG side wall after RIE all the way to the silicon Substrate.

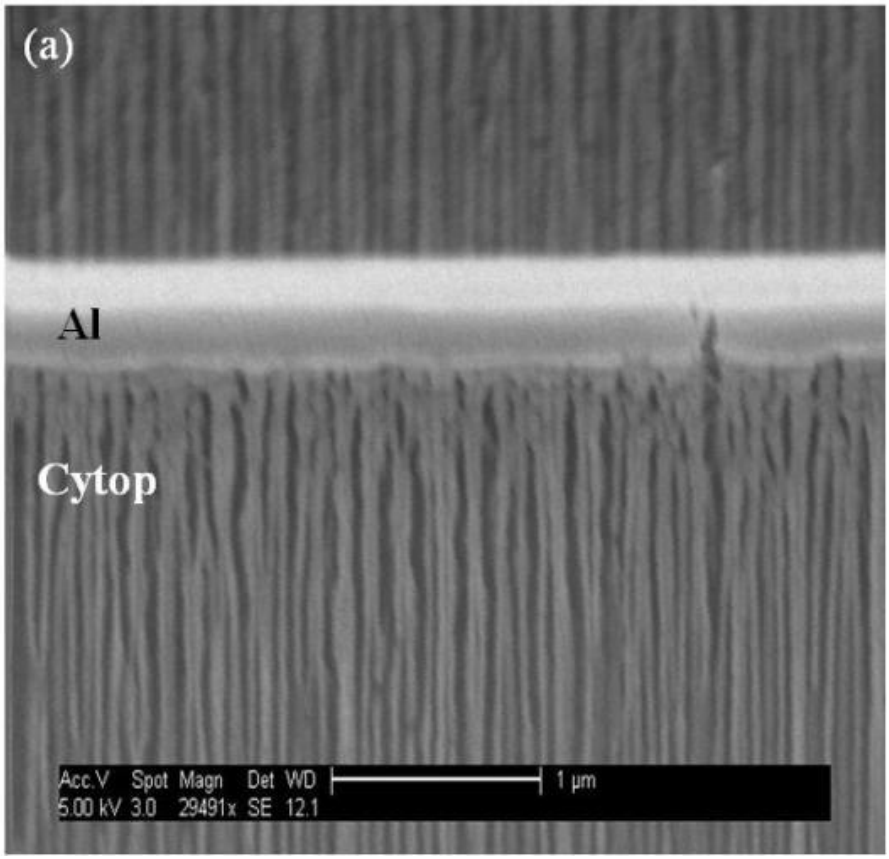

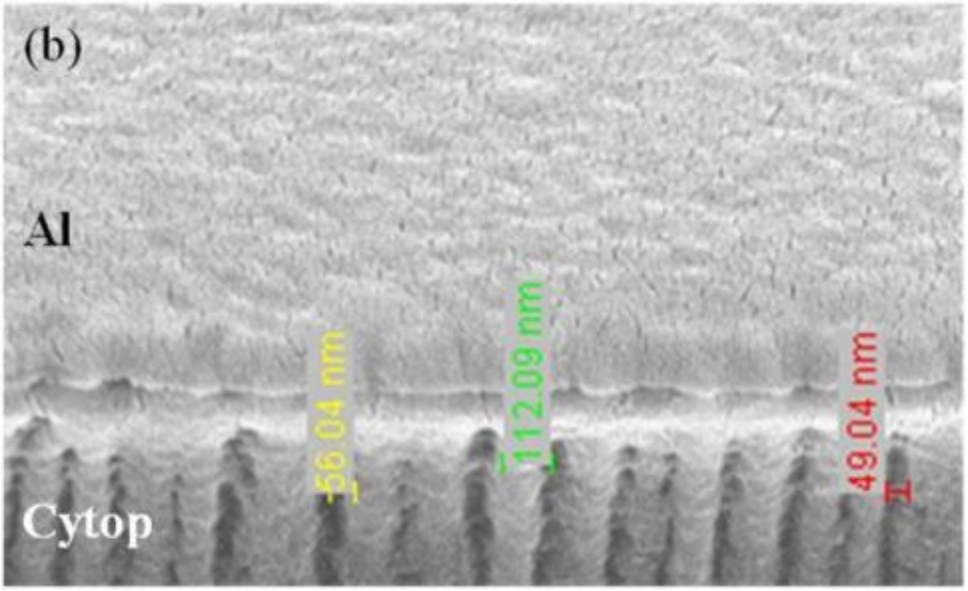

Figure 38: (a) and (b) waveguide side wall with roughness on the 100nm scale.

Step 7 to 9 all contribute to the narrowing of the waveguides width. The light exposure and development in the lithography Step, the Aluminum wet etch step and the RIE process. This narrowing should be considered in the mask design in order to achieve the required waveguide width.

Figure 39 shows a 10µm waveguide as it goes through the steps. After the Aluminum wet etch it was hard to obtain a good focus on the sample with an optical microscope as well with a SEM, due to the thin metallic layer. The images were calibrated with the constant period distance between neighboring waveguides that should remain the same as in the mask design. Figure 40 shows the waveguides width after steps 7 to 9 versus mask design width. It can be seen that the narrowing is constant for all widths and for all steps.

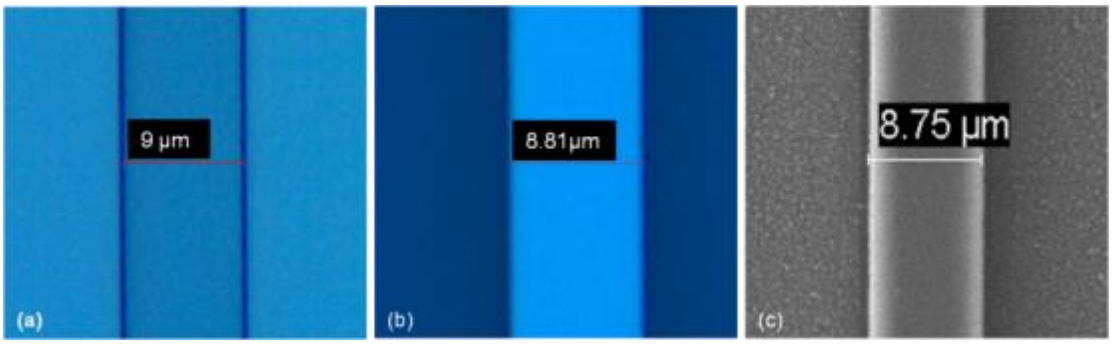

Figure 39: 10µm waveguide (a) after lithography Step (b) after aluminum wet etch Step (c) after RIE process.

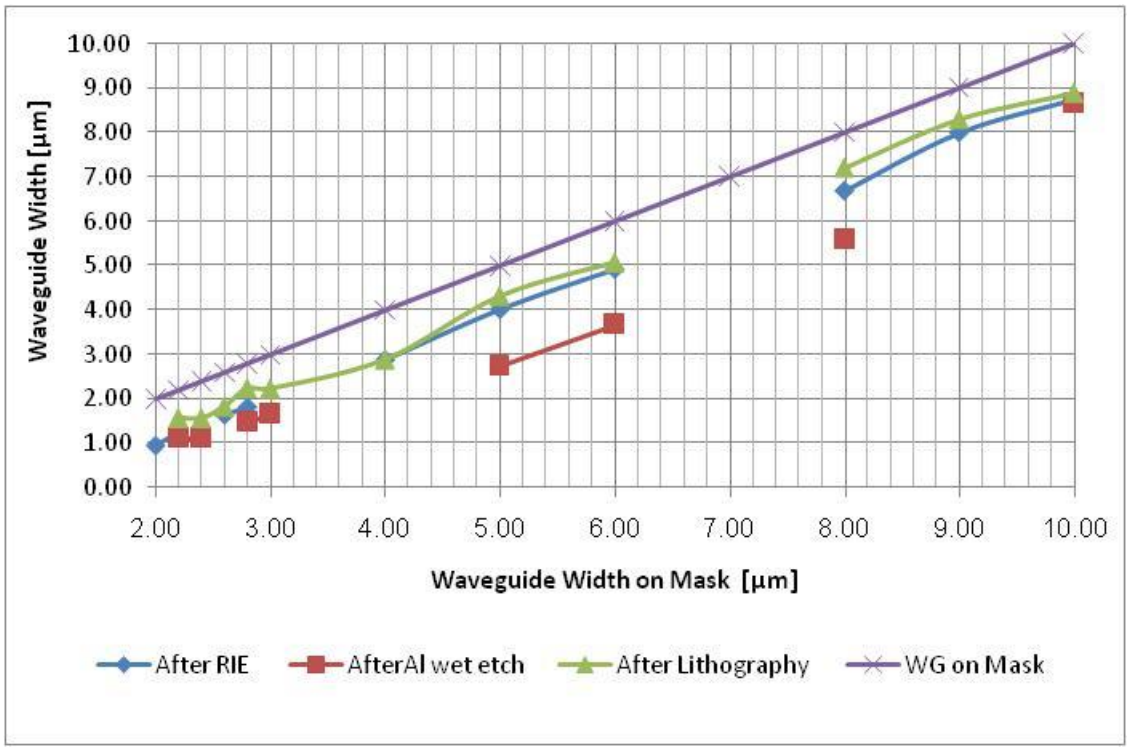

Figure 40: waveguide width after steps 7 to 9 to mask design width

Step 10 – Aluminum hard mask removal

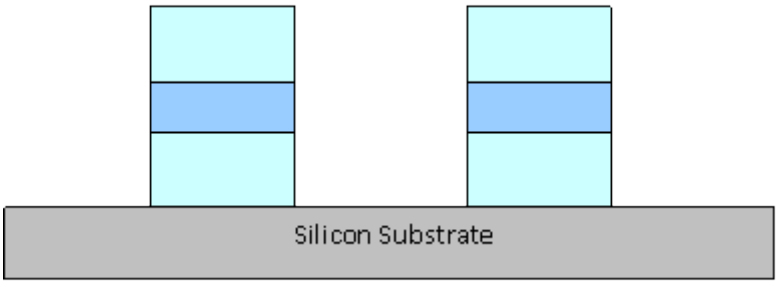

Removing of the Aluminum hard mask failed. The wet etch procedure attacked the PMMA core and damaged the waveguides.

Step 11 – Cytop Overall Coating

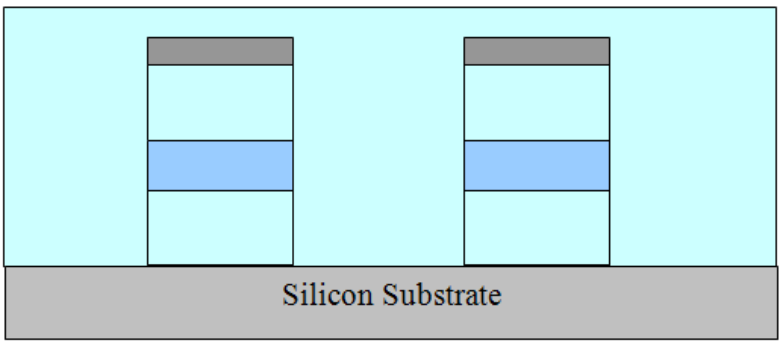

To produce symmetric signal wave mode in the waveguide, it is necessary that the core will be covered with the same refractive index material from all sides. Moreover it is essential to protect the waveguide channels from moisture, dust, or other physical damage. To improve the long-term stability, the addition of a cladding layer is essential. A simple spin-coat and curing, the same as in step 2, was done. Once again in this final step difficulties occur. At the end of the curing it is seen that the Aluminum hard mask peeled off the waveguide channel and the waveguides themselves moved from their original position (Figure 41 Figure 42). This thermal tension behavior has been seen before when a SU8 waveguide was covered under Cytop cladding. Solution was not yet found and we will be compelled to stay with air side walls or water with a refractive index of 1.3.

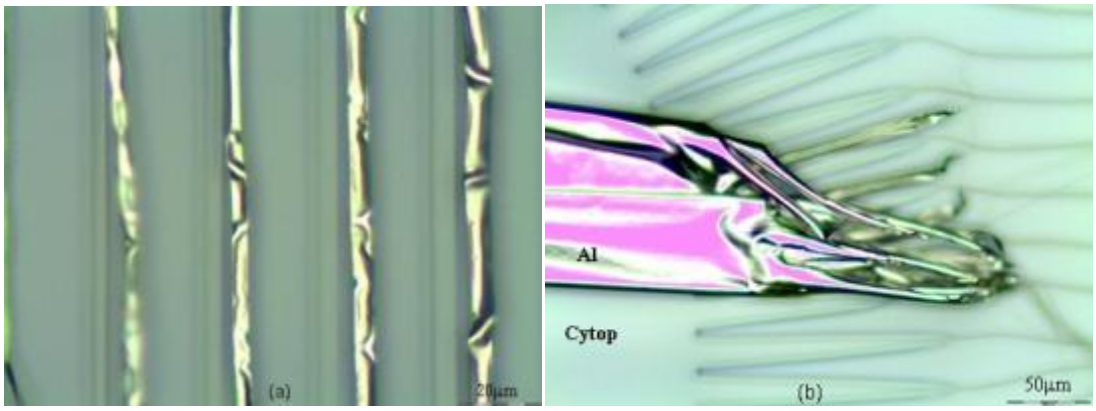

Figure 41: microscope Image result of Cytop coating upon the WG structures

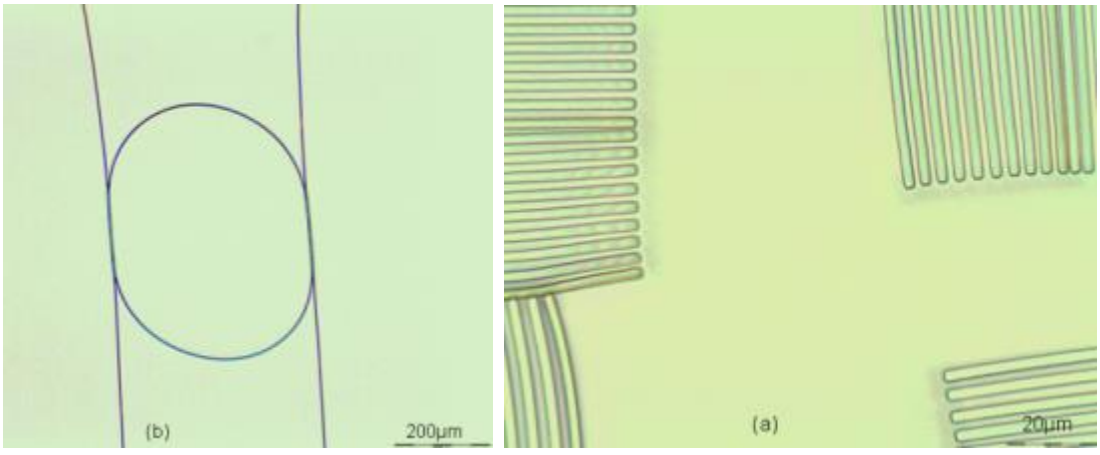

Figure 42: microscope Image result of Cytop coating upon the SU8 WG structures.

Step 12 – Dicing and Polishing or Cleaving

For the final stage of separating the devices, a dicing system with a 10um diamond saw and water cooling is used. Polishing the edges is done in six steps of polishing sheets from 50μm to 1μm. Figure 43 shows a polished silicon wafer with the polished layer of polymer on the top. Since there is no topography difference between the waveguide core and the cladding, the waveguides are not visible in the SEM image.

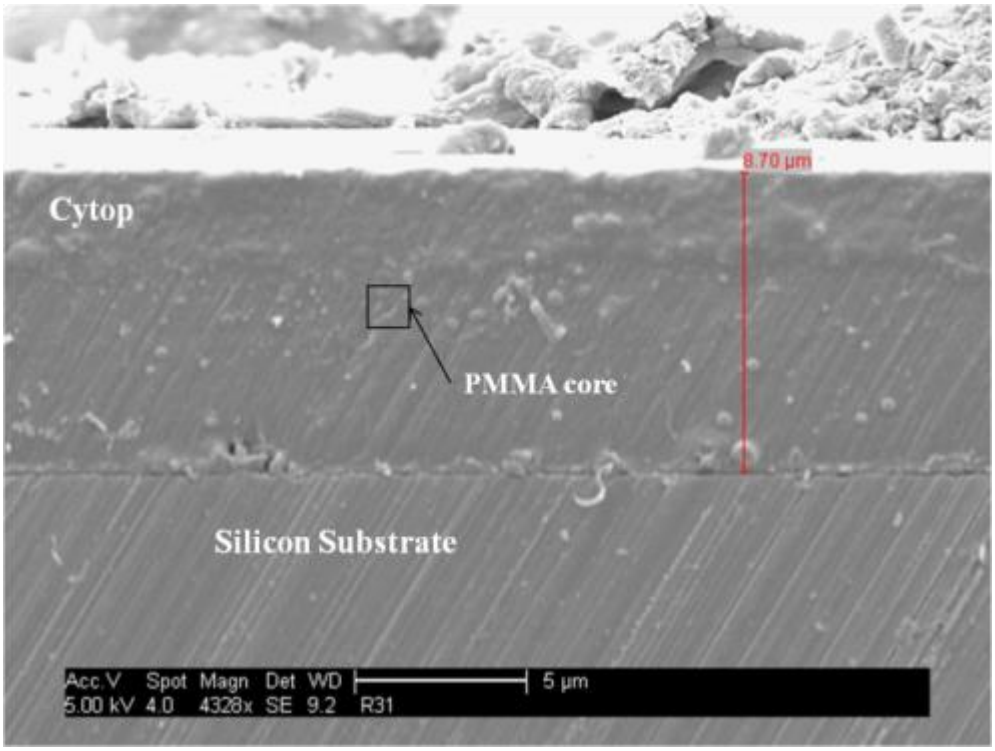

Figure 43: polished silicon wafer with the polished layer of polymer on the top

Cleaving can be used as well. To cleave the waveguide with a clean cut it is necessary to freeze the high flexible polymer first. We dipped the wafer in liquid nitrogen and then cleaved the silicon wafer (Figure 44).

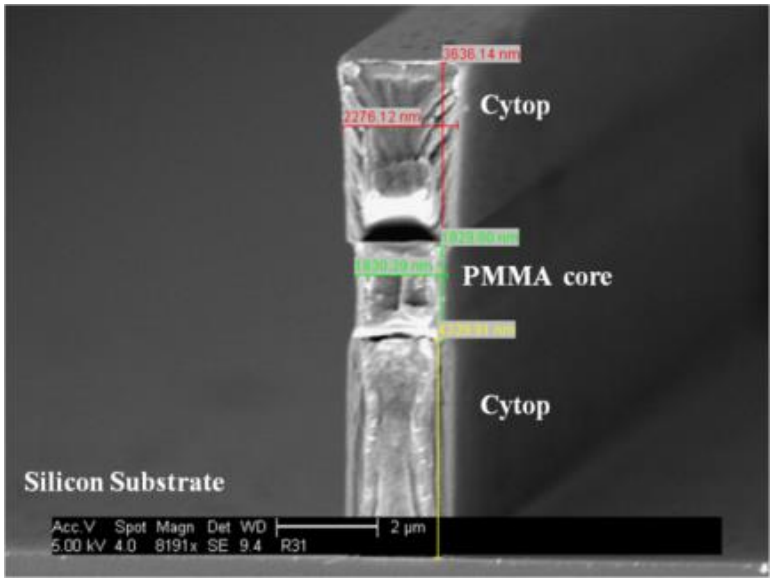

Figure 44: waveguide after cleaving

This project is still ongoing and at this point of time we have presented the difficulties in our journey of the fabrication process development. Figure 45 present our fabrication results, here we can see the triple-layer stack waveguides with Cytop under clad and over clad with a PMMA core. Figure 45 present the waveguide as light is coupled.

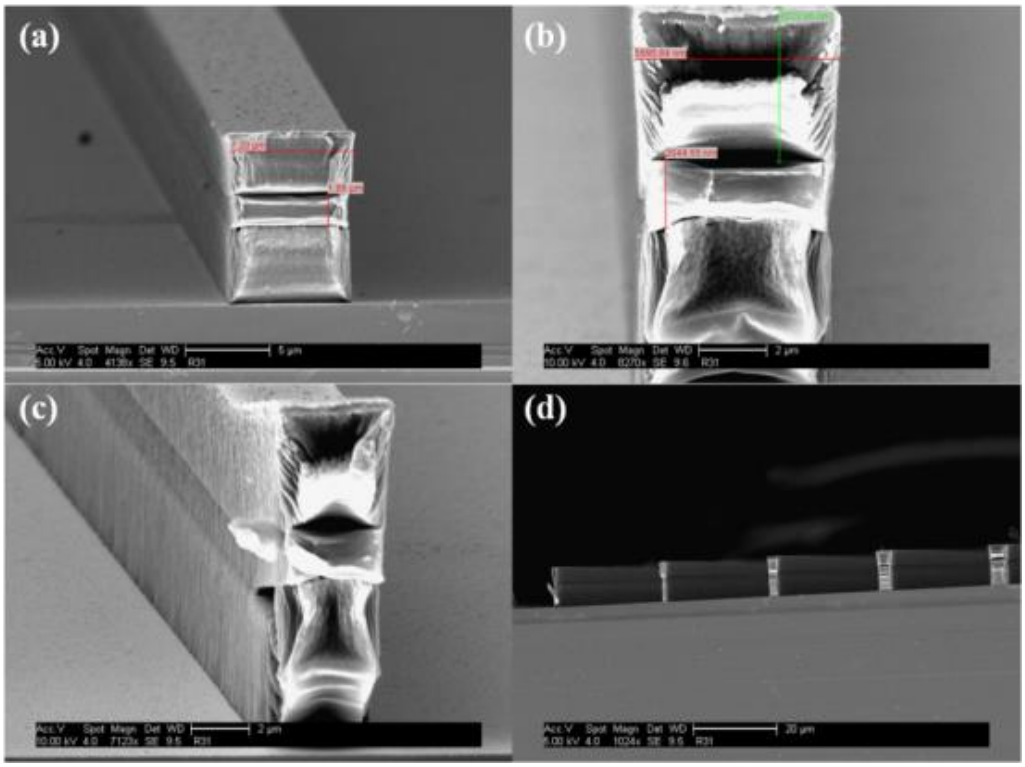

Figure 45: PMMA core with Cytop upper and lower cladding (a) 7µm waveguide (b) 6µm waveguide (c) 2µm waveguide (d) general view on waveguides test array.

Figure 46: light coupled in to a waveguide.

3.2.2 PFCB Core Waveguide using PECVD

In this fabrication process, most steps are the same as in the PMMA process. The major advantage using PECVD is that we can now deposit Silica on polymers. The 40nm silica layer at step 3 helped us to spin coat the PFCB core layer as it improved the adhesion to the Cytop surface. As this layer is very thin it shall not affect the optical mode. PFCB is spin coated and then cured overnight in an inert environment oven. The quality and reliability problems of the metallic hard masks vanished when a silica hard mask was used. As silica has a reflective index of 1.47 and PFCB's reflective index is 1.47, we chose to deposit the hard mask directly on the waveguide core. Figure 48 demonstrates the PFCB core waveguide process flow. To avoid movements of devices at the last over cladding step, we stopped the etching process to construct a ridged waveguide. This method proved to be successful as it binds the devices as one robust structure. Although, stress are still a problem in this over clad step as can be seen in Figure 50. Here we can see that the over clad congregate from the stress that are involved in the layers baking step at 120^{o}C (minimum baking temperature as manufacturer suggests). Surprisingly there were no strands left on the PFCB. The etch rate is 600nm/min. The waveguide roughness is about 100nm as well (Figure 49) In Figure 47 we see a SEM image of the PFCB core waveguide.

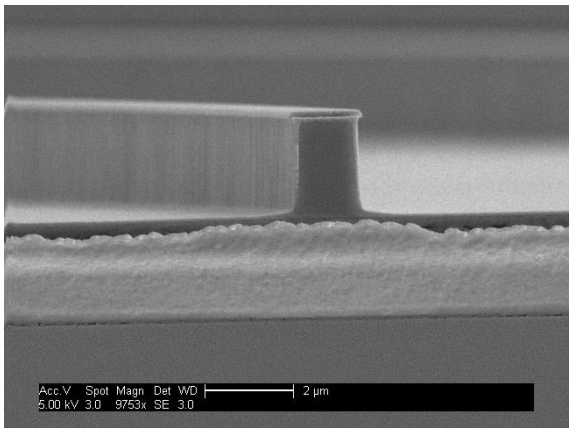

Figure 47: PFCB waveguide core after REI

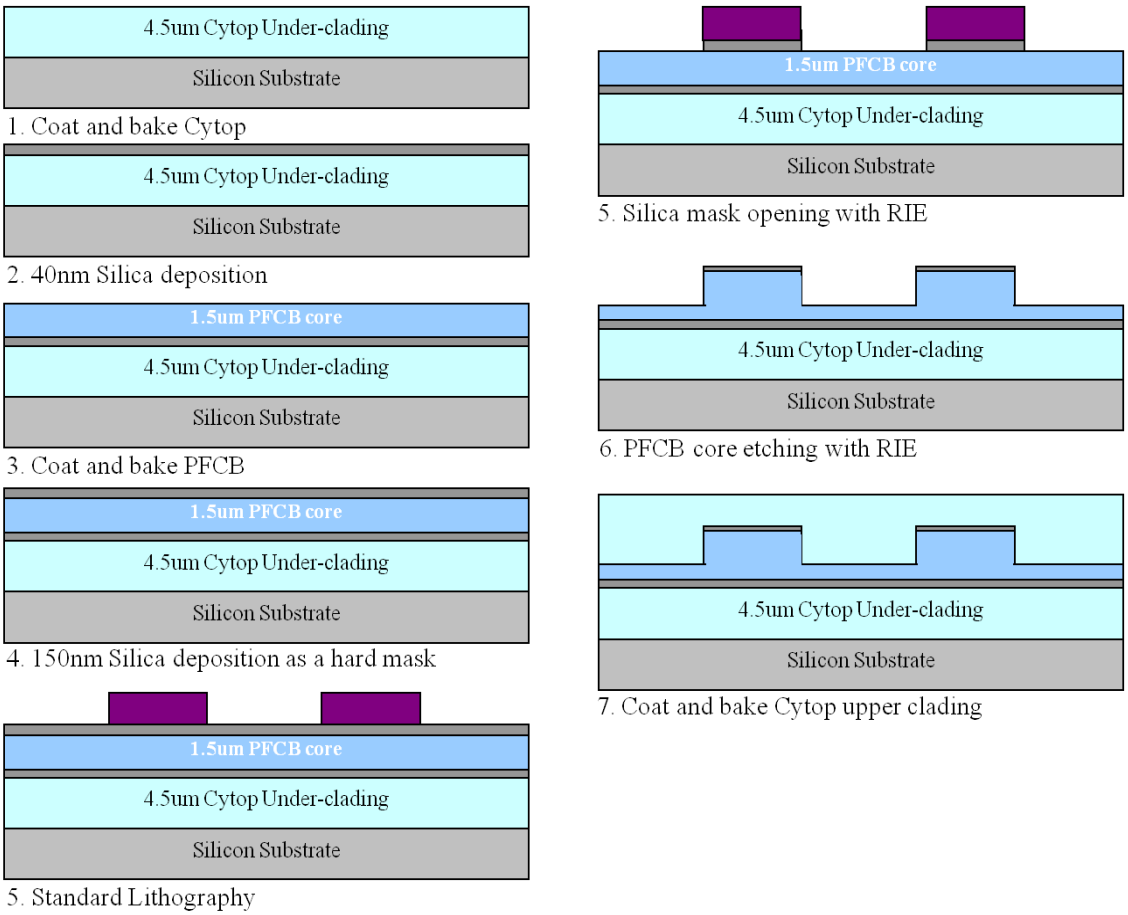

Figure 48: PFCB waveguide process steps

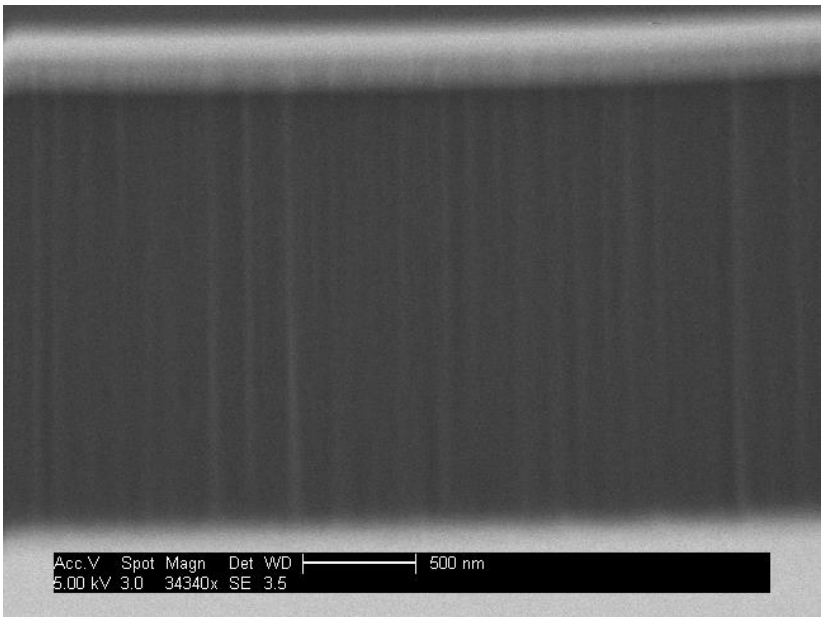

Figure 49 : Waveguide side view roughness is about 100nm.

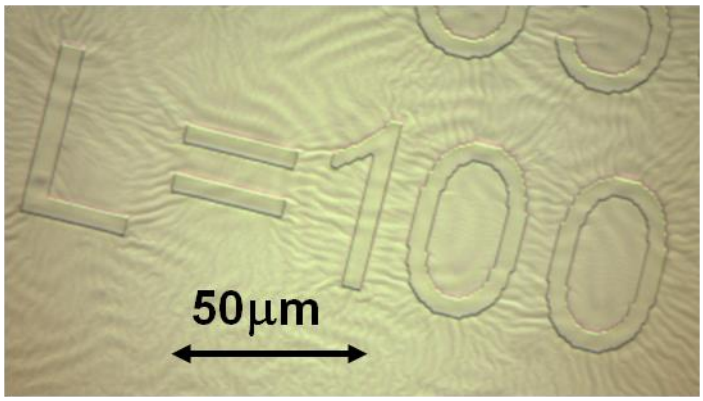

Figure 50 : Stress in Cytop over-clad

3.3 Additional Process

3.3.1 Electron-Beam Lithography

Waveguide fabrication with electron-beam lithography in PMMA with Cytop under clad was reported before [30]. In the early stages of our work the nanofabrication facility was still under construction and we decided to try the new ultra High Resolution Electron Beam Lithography system. This process should be easier then the main process flow.

PMMA is a positive resist; the electron beam writing defined the cladding regions. Electron-beam power dosage can be calibrated in few experiments. Limited electron beam scan deflection range is overcome by combination of stage movement and e-beam scanning. Large pattern of mm or cm size are divided into smaller fields, typically of 50, 100 or 200 µm and exposed in serial mode to reconstruct the original sized pattern. This is called stitching. Stage movement is 50, 100 or 200 µm to adjacent field. The remaining error along the small field borders due to stage positioning and distortion of beam deflection is called stitching error. Stitching error were the downfall, in our system it is impossible to move the stage when the Electron-beam power is on. Therefore it is very hard to make long devices on the centimeter scale.

Our initial design was a basic waveguide with tapers. The device structure is shown schematically in Figure 51. At Figure 52 Stitching error can be seen.

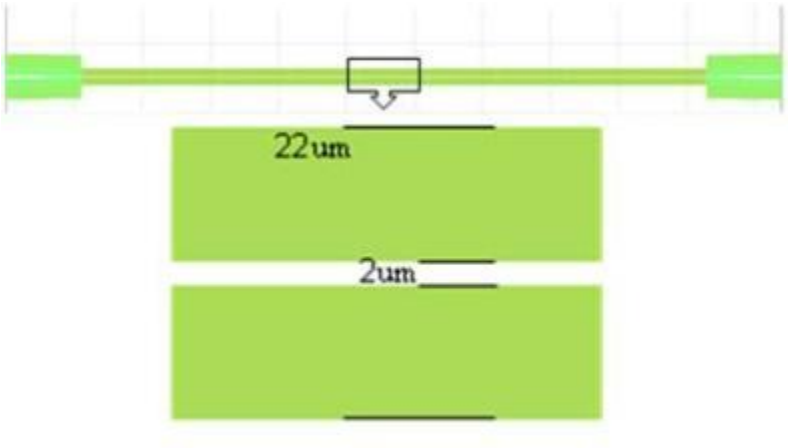

Figure 51: Device structure.

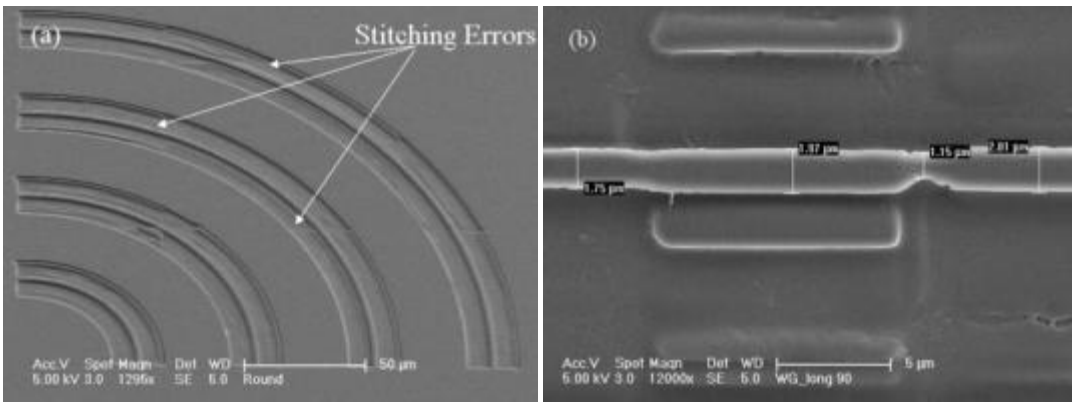

Figure 52: SEM Image result Stitching error of electron-beam lithography in PMMA with Cytop under clad.

3.3.2 Channel Dissolve Method

Due to difficulties that accrued during the hard mask step and poor accessible to the RIE system at Tel Aviv University an additional process was initiated. The process flow is shown schematically in Figure 53. In this process we used the difference of the chemical resistance between Cytop and the AZ photoresist. Cytop has a very good chemical resistance to solvents. To achieve this process a RIE system is required as well for its homogenous etching abilities. For now this process was abandoned. It might be tested again in the future.

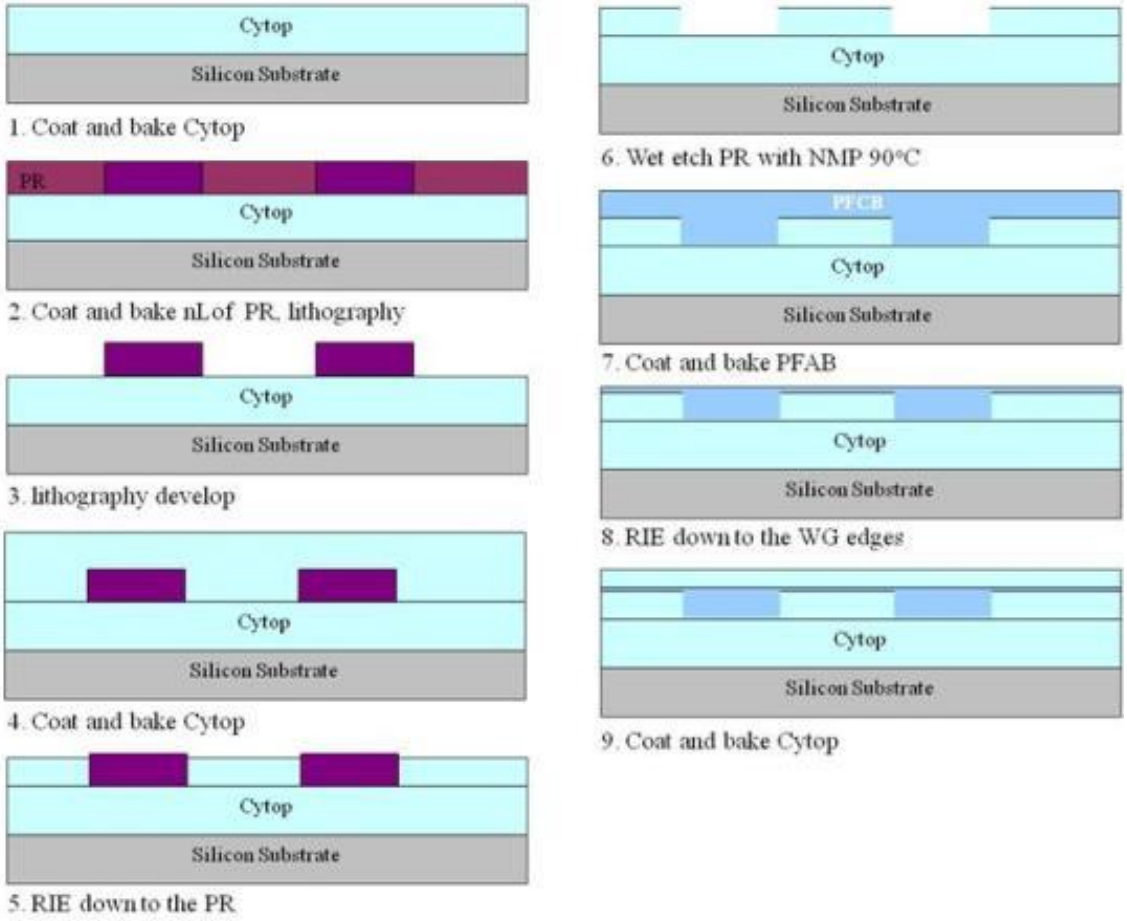

Figure 53: Channel dissolves method process flow

Chapter 4

Summary and Discussion

We have demonstrated the design and simulations as well as fabrication and process development of various polymer-based waveguide devices. This work demonstrates a new combination of polymer materials to construct a waveguiding platform that is optimized for the common telecommunications wavelengths and can be doped with semiconductors nanocrystals. We used both PMMA and PFCB polymers as core materials and Cytop polymer as cladding. Two simulation techniques were used to design and optimize critical parameters of these devices; the beam propagation method and the plane wave expansion method. In this project, procedures of fabrication based on spin-coating and RIE techniques have been studied and optimized for achieving the device structures.

During the process development stage we encountered many obstacles, whose resolution required careful attention to detail. Adhesion problems are known to occur when dealing with Flouropolymers. When directly deposited on a silicon wafer, it is preferred to find a chemical solution for surface preparation. In our case a Silane treatment proved successful. For adhesion to a previous polymer layer a chemical solution is preferred, for its smooth and homogeneous interface results. Alternatively a short O_2 plasma etching process as a surface treatment can be used for opening surface bonds to improve adhesion. This solution is sub-optimal, as it leaves an uneven layer which induces light scattering, leading to optical losses at the

waveguide's upper and lower core-cladding interfaces. This effect can be effectively minimizing by shortening the O_2 RIE process to achieve a more homogenous result.

Stress management in the fabrication process proved important as well. The materials that are needed in achieving the final devices have significant differences in their coefficients of thermal expansion (CTE) and are exposed to different temperatures throughout the process. Cracks, congregates and movement of devices have been the main problem through out all the process development steps. Lowering the preparation temperature and means of slow ramping to the required temperature can solve most problems. Devices movement was dealt by changing the device structure from buried to ridged waveguide. This method proved to be successful as it binds the devices as one robust structure. Moreover, low preparation temperature is useful when heat-sensitive elements, such as semiconductors nanocrystals, are to be embedded in the waveguide.

The polymer waveguide structure can be processed in one of two means. The first utilizes a chemical dissolving process that can be done with SU8 or PMMA. SU8 is sensitive to UV light and can be designed with a simple lithography procedure and PMMA is sensitive to electron beam writing. These lithography methods do not leave their mark on the waveguide as sidewall roughness, which contributes to optical losses from the waveguide sidewall core-cladding interface. Therefore, when optical devices are constructed these methods are preferred. The second option is based on a RIE procedure as we used in our fabrication process. This RIE procedure will leave its mark as sidewall roughness, as has been showed in the previous chapter. Therefore, it is recommended to address the sidewall roughness by finding a method to reduce it. A brief chemical immersion in a solvent or acid could smooth the sidewall roughness.

Dicing, polishing and cleaving techniques should be studied and improved as well. The elasticity of our polymeric medium can make these procedures difficult. Freezing the polymer with liquid nitrogen proved successful for the PMMA waveguide, as shown in Figure 44. Dicing and then polishing can be done but it is hard to achieve with an elastic polymer. In our design, the waveguide edges ended at the dicing line, as we attempted a dicing polishing method. Ending the waveguides with no dicing line will help us to cleave the silicon wafer near the waveguides edges without

needing a polish, as the RIE roughness will still be much better than any polishing technique.

Our goal waveguide dimensions for the various devices, such as ring resonators, couplers etc., was 1.5μm. Fabrication steps such as lithography and RIE contributes to the thinning of the waveguides beneath the goal width. To obtain this goal, it is desired to design the waveguide devices on the lithography mask with widths of 2.8μm.

In addition to these issues, designing polymeric structures in micron-scale requires delicate care. Slowly pouring of the polymer solution on to the silicon wafer at the spin coating step, is essential to avoid bubbles and an inhomogeneous layer. Clean working methods beyond the clean room environment are important to maintain the low defect tolerance of long micron-scale waveguide. These are just the few examples of the delicate working methods that are required for successfully fabricating polymer waveguides. Our project is still ongoing within our research group, and will continue to pursue the research core goal of nanocrystals embedment.

Bibliography

1. Okamoto, K., Fundamental of Optical Waveguides. Optics and Photonics. 2000, San Diego: Academic Press.

2. Bruchez M, Moronne M, Gin P, Weiss S, and Alivisatos AP, "Semiconductor nanocrystals as fluorescent biological labels", Science, 281, 2013, 1998.

3. S. Coe, W. K. Woo, M. G. Bawendi, and V. Bulovi, "Electroluminescence from single monolayers of nanocrystals in molecular organic devices", Nature (London) 420, 800, 2002.

4. V. I. Klimov, A. A. Mikhailovsky, S. Xu, A. Malco, J. A. Hollingsworth, C. A. Leatherdale, H.-J. Eisler, and M. G. Bawendi, "Optical Gain and Stimulated Emission in Nanocrystal Quantum Dots," Science 290, 314-317, 2000.

5. Klimov VI, Mikhailovsky AA, McBranch DW, Leatherdale CA, "Quantization of multiparticle auger rates in semiconductor quantum dots", Science 287 (5455), 1011, 2000.

6. Oron D, Kazes M and Banin U, "Multiexitons in Type-II Colloidal Semiconductor Quantum Dots", Phys. Rev. B 75, 035330 (2007).

7. O. Millo, D. Steiner, D. Katz, A. Aharoni, S. Kan, T. Mokari, and U. Banin, “Transition from zero-dimensional to one-dimensional behavior in InAs and CdSe nanorods,” Physica E 26, pp. 1-8 , 2005.

8. J. T. Hu, L. S. Li, W. D. Yang, L. Manna, L.W. Wang, and A. P. Alivisatos, “Linearly polarized emission from colloidal semiconductor quantum rods,” Science 292, pp. 2060-3, 2001.

9. Harrison MT, Kershaw SV, Burt MG, Rogach AL, Kornowski A, Eychmüller A, and Weller H, "Colloidal nanocrystals for telecommunications. Complete coverage of the low-loss fiber windows by mercury telluride quantum dots", Pure Appl. Chem., Vol. 72, Nos. 1–2, pp. 295–307, 2000.

10. Persans PD, Huang F, Agarwal N, Ponoth S, and Plawsky JL, "Dielectric materials in optical waveguide applications", in Interlayer Dielectrics for Semiconductor Technologies, p 349 - S. Murarka, M. Eizenberg, A. Sinha editors (Elsevier, 2003)

11. Ballato J, Foulger SH, Smith DW Jr., "The Optical Properties of Perfluorocyclobutyl Polymers II: Theoretical and Experimental Performance", JOSA B, Vol. 21, Issue 5, pp. 958-967 (2004).

12. Y. K. Olsson, G. Chen, R. Rapaport, D. T. Fuchs, V. C. Sundar, J. S. Steckel, M. G. Bawendi, A. Aharoni, and U. Banin, “Fabrication and optical properties of

polymeric waveguides containing nanocrystalline quantum dots," Appl. Phys. Lett. 85, pp. 4469-71, 2004.

13. L. Pang, Y. M. Shen, K. Tetz, Y. Fainman, "PMMA quantum dots composites fabricated via use of pre-polymerization," Opt. Expr. 13, pp. 44-49, 2005.

14. Zhao, Y.G., et al., Polymer waveguides useful over a very wide wavelength range from the ultraviolet to infrared. Applied Physics Letters, 2000. 77(19): p. 2961-2963.

15. Marcatil.Ea, Bends in Optical Dielectric Guides. Bell System Technical Journal, 1969. 48(7): p. 2103.&-

16. Heiblum, M. and J.H. Harris, Analysis of Curved Optical-Waveguides by Conformal Transformation. Ieee Journal of Quantum Electronics, 1975. Qe11(2): p. 75-83.

17. Doerr, C.R. and H. Kogelnik, Dielectric waveguide theory. Journal of Lightwave Technology, 2008. 26(9-12): p. 1176-1187.

18. Smink, R.W., B.P. de Hon, and A.G. Tijhuis, Bending loss in optical fibers - a full-wave approach. Journal of the Optical Society of America B-Optical Physics, 2007. 24(10): p. 2610-2618.

19. Dragone C, "Optimum Planar Bends" Electronics letters, Vol. 29 No. 29 pp. 1121-1122, 1993

20. E. Rothenberg, M. Kazes, E. Shaviv, and U. Banin, "Electric field induced switching of the fluorescence of single semiconductor quantum rods," Nano Lett. 5, pp. 1581-6, 2005.

21. L. B. Soldano and E. C. M. Pennings, "Optical Multi-Mode Interference Devices Based on Self-Imaging : Principles and Applications," IEEE Journal of Lightwave Technology, Vol 13, No. 4, pp. 615-627, 1995.

22. Bosc, D., et al., Investigation into defects occurring on the polymer surface during the photolithography process. Applied Surface Science, 2007. 253(14): p. 6162-6164.

23. Kagami, M., et al., Fabrication of Large-Core, High-Delta Optical Wave-Guides in Polymers. Applied Optics, 1995. 34(6): p. 1041-1046.

24. Soldano, L.B. and E.C.M. Pennings, Optical Multimode Interference Devices Based on Self-Imaging - Principles and Applications. Journal of Lightwave Technology, 1995. 13(4): p. 615-627.

25. Yariv, A., Universal relations for coupling of optical power between microresonators and dielectric waveguides. Electronics Letters, 2000. 36(4): p. 321-322.

26. T. K. Lim, B. K. Garside, J. P. Marton, "An Analysis of Optical Waveguide Tapers" Applied Physics, Vol. 18, pp. 53-62, 1979

27. Theodore H. Fedynyshyn,' Gregory W. Grynkewich, "The Effect of Aluminum *vs.* Photoresist Masking on the Etching Rates of Silicon and Silicon Dioxide in CF4/02 Plasmas" *J. Electrochem. Soc.Vol. 134, No. 1* pp. 206-209, 1987

28. Poon, J.K.S., et al., Polymer microring coupled-resonator optical waveguides. Journal of Lightwave Technology, 2006. 24(4): p. 1843-1849.

29. Manabu Kagami, Hiroshi Ito, Tadashi Ichikawa, Satoru Kato, Morihiro Matsuda. "Fabrication of large-core, high-Δ optical waveguides in polymers" Applied Optics. Vol. 34, No. 6 pp. 1041-1046, 1995

30. Joyce K. S. Poon, Lin Zhu, Guy A. DeRose, Amnon Yariv, "Transmission and group delay of microring coupled-resonator optical waveguides" Optics Letters. Vol. 31, No. 4, pp. 456-458, 2006

מוליכי גלים פולימריים חדשניים המיועדים לאכלוס בננו-גבישים

עבודת גמר לתואר מוסמך

מוגש על ידי

ירון גלזר

בהנחיית דוקטור דן מרום

האוניברסיטה העברית בירושלים - הפקולטה למתמטיקה ולמדעי הטבע

בית ספר להנדסה ומדעי המחשב - המחלקה לפיסיקה יישומית

November 23, 2008

תקציר

לאורך העשור האחרון חל גידול עז בתעבורת האינפורמציה בעולם. הדבר הביא לצורך בתקשורת אופטית בשל יכולות התעבורה הגבוהה שלה. המהפכה האמיתית בתקשורת האופטית נוצרה כתוצאה מהזמינות של סיבי סיליקה בעלי הפסדים נמוכים מאוד. כמו כן, סיליקה משמשת כאבן הבניה לרכיבים אופטיים רבים אחרים. אולם, רכיבים אופטיים פסיביים עשויים מסיליקה ומזכוכית, או רכיבים אקטיביים שמנצלים את פער האנרגיה במוליכים למחצה, הם בעלי עלות יצור גבוהה.

מטרת המחקר שלנו היא לייצר מוליכי גלים אופטיים מפולימרים פסיביים ובעתיד לאלח אותם בננוגבישים ממוליכים למחצה. יש לומר כי רכיבים אופטיים המשתמשים בחומרים פלסטיים מצויים כיום באופן ניכר בשוק הטלקומוניקציה.

בעבודה זו אנו מציגים את התכנון והיצור של רכיבים אופטיים אלו. קשרי הפחמן-חמצן וקשרי חנקן-הליום המצויים ברוב הפולימרים הם בעלי בליעה גבוהה באורך הגל של התקשורת האופטית 1.55 מיקרון. לשם כך יש לבחור בקפידה את הפולימרים המתאימים. הפולימרים שנבחרו במחקר זה הם PFCB לליבה ו- Cytop למעטפת, ומורכבים לכדי מוליך גל זו הפעם הראשונה במחקר ידוע. פולימרים אלו הם בעלי בליעה נמוכה באורך הגל המבוקש.

בתכנון הרכיבים שמנו דגש מיוחד על רכיבים אופטיים שיוכלו לעזור לחלץ את התכונות האופטיות של הרכב פולימרים חדש זה, כגון: הפסדים בהולכה, הפסדים בסיבובים ושינויים במקדם השבירה, שצפויים להתרחש לאחר האילוח בננוגבישים.

מוליכי גלים בעלי חתך צד של מיקרון ואורך של מספר סנטימטרים רגישים במיוחד לפגמים בתהליך היצור. יצור הרכיבים נעשה באמצעות תהליכים סטנדרטים מעולם הפבריקציה של המוליכים למחצה, כגון ליטוגרפיה, עיכול יבש וכדומה. כמו כן, יצור הרכיבים בטמפרטורות נמוכות הינו הכרחי בשל הימצאותם של רכיבים רגישים לחום, כגון הננוגבישים. כעת, לאחר סיום פיתוח התהליך, התקבלו מוליכי הגלים הרצויים אשר מוכנים לאילוח בננוגבישים במחקר עתידי.